

## The Fate of Oxygen in the Ocean and Its Sensitivity to Local Changes in Biological Production

Mark Holzer<sup>1</sup> 

<sup>1</sup>Department of Applied Mathematics, School of Mathematics and Statistics, University of New South Wales, Sydney, NSW, Australia

### Key Points:

- We map out where the oxygen deficit of low-oxygen regions originates and link deficit and utilization rates with a new mean transport time
- The sensitivity pattern of low-oxygen regions to production changes is shaped by the time to next ventilation spent in the regions
- In and below the hypoxic North Pacific 70%–90% of the oxygen concentration will get utilized before next ventilation

### Correspondence to:

M. Holzer,  
mholzer@unsw.edu.au

### Citation:

Holzer, M. (2022). The fate of oxygen in the ocean and its sensitivity to local changes in biological production. *Journal of Geophysical Research: Oceans*, 127, e2022JC018802. <https://doi.org/10.1029/2022JC018802>

Received 17 NOV 2021

Accepted 25 JUL 2022

**Abstract** We investigate the sensitivity of the oxygen content and true oxygen utilization of key low-oxygen regions  $\Omega$  to pointwise changes in biological production. To understand how the combined water and biogenic particle transport controls the sensitivity patterns and the fate of oxygen in the ocean, we develop new relationships that link the steady-state oxygen content and deficit of  $\Omega$  to the downstream and upstream oxygen utilization rate (OUR), respectively. We find that the amount of oxygen from  $\Omega$  that will be lost per unit volume at point  $\mathbf{r}$  is linked to OUR( $\mathbf{r}$ ) through the mean oxygen age accumulated in  $\Omega$ . The geographic sensitivity pattern of the  $\Omega$ -integrated oxygen deficit is shaped by where the utilization occurs that causes this deficit. The contribution to the oxygen deficit of  $\Omega$  from utilization at  $\mathbf{r}$  is controlled by the mean time that water at  $\mathbf{r}$  spends in  $\Omega$  before next ventilation at the surface. We illustrate these relationships and the new transport timescales using a simple steady-state data-constrained carbon and oxygen model. We focus on  $\Omega$  being the global ocean, the Pacific Hypoxic Zone (PHZ,  $[\text{O}_2] < 62.5 \mu\text{M}$ ), and the North Pacific oxygen minimum zone. The oxygen deficit of the PHZ is most sensitive where mode and intermediate waters form and where increased organic-matter production directly increases the PHZ's oxygen demand. The fraction of the local oxygen concentration that will be utilized in respiration is as high as 90% in the PHZ and up to 70% in the water column beneath it.

**Plain Language Summary** Dissolved oxygen is vital for marine animals. Oxygen in the ocean comes primarily from the atmosphere and is consumed throughout the water column by microbes that break down organic matter produced by photosynthesis near the surface. In certain parts of the ocean interior, where oxygen consumption is high and the supply of freshly oxygenated waters is low, the oxygen concentration is lethally low for many animals. As the surface production of organic matter changes due to environmental factors, so does the oxygen demand in the ocean interior. Here we develop new relationships for understanding the fate of oxygen in the ocean and illustrate them with an ocean model. By tracing the oxygen deficit of a given subsurface region back in time to where the oxygen was consumed, we show that the sensitivity of the region's oxygen content to changes in biological productivity is controlled mainly by the time water spends in the region before getting re-oxygenated at the surface. By tracing oxygen forward in time to where it gets utilized, we show that 70%–90% of the oxygen in the North Pacific below a few hundred meters depth gets utilized in the breakdown of organic matter.

## 1. Introduction

Oxygen is essential for most life in the ocean and forms a central component of global ocean biogeochemical cycles by controlling the respiration of organic matter, the chemical state of trace metals, and thus the ocean's carbon and nutrient cycles. The key factors controlling the oxygen content of the ocean are temperature-dependent solubility and air-sea exchange, stratification-dependent ventilation, and organic-matter photosynthesis and respiration, all of which are likely to change in the future. Observational evidence points to the ocean's oxygen content having decreased by order 1% over recent decades (e.g., Helm et al., 2011; Whitney et al., 2007), and to very large changes over geologic history (e.g., Keeling et al., 2010, and references therein). Past global warming during the late Permian has been linked to marine mass extinctions (Penn et al., 2018), and models suggest that future warming and circulation changes could expand oxygen deficient zones and reduce the ocean's oxygen content by 2%–12% by the end of the 21st century (e.g., Matear et al., 2000; Oschlies et al., 2008) and by as much as ~30% in the deep ocean over the next several hundred years and beyond (Matear & Hirst, 2003; Schmittner et al., 2008; Moore et al., 2018). Simulations of oxygen under the Representative and Extended Concentration Pathway 8.5 future  $\text{CO}_2$  scenarios have shown that increasing tropical hypoxia could eventually reverse mainly

© 2022. The Authors.

This is an open access article under the terms of the [Creative Commons Attribution-NonCommercial-NoDerivs License](https://creativecommons.org/licenses/by/4.0/), which permits use and distribution in any medium, provided the original work is properly cited, the use is non-commercial and no modifications or adaptations are made.

through weakened tropical organic-matter export (Fu, Primeau, et al., 2018). Simulations under doubled CO<sub>2</sub> conditions have suggested that deoxygenation could stabilize not just because of reductions in respiration but also from the reduction of undersaturated water masses formed at high latitudes, highlighting the potential importance of future circulation changes (Palter & Trossman, 2018). In the current climate, the North Pacific is of particular interest as a large volume in the upper ~2 km has hypoxic conditions lethal for many higher organisms (Vaquer-Sunyer & Duarte, 2008), and the tropical eastern North Pacific contains the world's largest oxygen minimum zone (OMZ) where suboxia forces anaerobic microbial respiration using nitrate for oxidation. Because these low-oxygen regions are particularly sensitive to climate-driven changes they have been the focus of many studies (e.g., Karstensen et al., 2008; Stramma et al., 2008, 2010; Weber & Bianchi, 2020), and we will examine them further here.

The oxygen utilization rate (OUR) is key for understanding the global oxygen distribution as well as for modeling oxygen, nutrients, and carbon. Because the OUR is proportional to the rate of organic matter loss, the OUR integrated over the aphotic ocean provides a direct constraint on export production (e.g., Jenkins, 1982; Oschlies & Kähler, 2004; Primeau et al., 2013). Observationally, OUR is typically inferred from the apparent oxygen utilization (AOU) together with an age estimate to provide a rate (e.g., Emerson & Hedges, 2008; Jenkins, 1982; Sonnerup et al., 1999, 2015). Issues with this empirical approach related to undersaturated surface waters have been demonstrated (Ito et al., 2004), and because of its nonlinear temperature dependence the in situ saturation does not properly represent the admixture of saturation that traces back to the surface. Importantly, using a mean age to determine the local OUR also raises conceptual issues as this approach is more appropriate for a path-integrated utilization rate than for providing a measure of the local in situ respiration rate. The mean-age-based OUR rests on the idea of a purely advective Lagrangian parcel for which the age simply measures the transit time from the surface (e.g., Emerson & Hedges, 2008). One approach takes OUR as the ratio AOU/age (or the slope of the AOU vs. age regression) and another approach defines OUR as the ratio of isopycnal AOU and age gradients to obtain a more local measure of respiration rate (Sonnerup et al., 2013). However, as pointed out by Koeve and Kähler (2016), because mean age and AOU have different gradients they do not co-evolve or “age” in a proportional manner under the action of advective-diffusive transport. Consequently, age-based OUR metrics have been found to systematically underestimate the respiration rate (Koeve & Kähler, 2016).

Here we use a simple data-constrained model of the global climatological oxygen and carbon cycles to investigate the sensitivity of oxygen to changes in biological production. We focus on the response of regional budgets to point-wise perturbations in euphotic biological production. The regions considered are: the global ocean, the North Pacific hypoxic zone (defined by observed [O<sub>2</sub>] < 62.5 μM), and the North Pacific oxygen minimum zone (NP OMZ, observed [O<sub>2</sub>] < 20 μM). By tracing true oxygen utilization (TOU, which is analogous to AOU but replaces saturated with preformed oxygen (Broecker & Peng, 1982; Ito et al., 2004)) back in time, we establish where the oxygen deficit of a given region originated, and by tracing oxygen forward in time we establish where it will next be utilized before being able to escape to the atmosphere. In the process, we develop new relationships between TOU, in situ OUR, and new mean transport times for water and oxygen that are useful conceptually and for diagnosing the oxygen sinks in biogeochemical models. We show that the sensitivity of regionally integrated TOU to changes in biological production is set dominantly by the upper-ocean structure of the mean water re-exposure time that was spent in the region of interest. (Note that re-exposure time, unconditioned on where it was spent, is the mean time to *next* surface contact, distinct from the mean age which is the mean time since *last* surface contact.)

In Section 2 we briefly describe the global model used to illustrate our new analyses of the ocean's oxygen cycle. This is followed by our results in Section 3 where key new diagnostic relationships are presented alongside the corresponding model results, with details provided in the Appendices A–D. Section 3.1 examines the model's oxygen field, Section 3.2 discusses the sensitivity of low-oxygen regions to changes in biological production, Section 3.3 explores the controls on the sensitivity patterns, and Section 3.4 quantifies the fate of oxygen in the ocean more broadly. We put our results into perspective and discuss key caveats in Section 4 and conclude in Section 5.

## 2. Oxygen Model and Labeling Tracers

### 2.1. Biogeochemical Model

We build on a simple data-constrained model of the ocean's phosphate and carbon cycles (Holzer, Kwon, & Pasquier, 2021) by adding a jointly optimized oxygen component. The model prescribes the functional forms for the particle-flux profiles (Najjar et al., 1992; Kwon & Primeau, 2008) and is embedded in a steady global ocean circulation using version 2 of the ocean circulation inverse model of DeVries (2014) (OCIM2, DeVries & Holzer, 2019). OCIM2 has a  $2^\circ \times 2^\circ$  horizontal resolution with 24 vertical levels and assimilates climatological air-sea heat and freshwater fluxes as well as mean sea-surface height, and the tracers temperature, salinity, CFC-11, CFC-12, natural radiocarbon, and natural  $\delta^3\text{He}$ .

Like the parent carbon and phosphate models, our simple oxygen model follows the approach of the Ocean Carbon-cycle Model Intercomparison Project (OCMIP, Najjar et al., 2007). The oxygen utilization rate (OUR, defined here as the in situ oxygen loss rate per unit volume) is provided by the respiration rate of semilabile dissolved organic carbon [DOC], which is fed by the rapid dissolution of particulate organic carbon [POC]. The oxygen sub-system analyzed here is given by

$$\begin{aligned} \partial_t [\text{O}_2] + \mathcal{T} [\text{O}_2] &= -\text{OUR} + R_{\text{O}_2:\text{C}} U_{\text{C}} + K_{\text{as}} ([\text{O}_2]_{\text{sat}} - [\text{O}_2]), \\ \partial_t [\text{DOC}] + \mathcal{T} [\text{DOC}] &= \sigma U_{\text{C}} + k_{\text{poc}} [\text{POC}] - \kappa_{\text{doc}} [\text{DOC}], \\ \partial_t [\text{POC}] + \mathcal{T}_{\text{poc}} [\text{POC}] &= (1 - \sigma) U_{\text{C}} - k_{\text{poc}} [\text{POC}]. \end{aligned} \quad (1)$$

where  $\mathcal{T}$  is the OCIM2 advective-eddy-diffusive flux-divergence operator, and  $\mathcal{T}_{\text{poc}}$  is the flux-divergence operator of sinking POC that dissolves with timescale  $k_{\text{poc}}^{-1}$ . POC is not advected with the flow here, but falls through the water column with a mean speed that increases linearly with depth yielding a Martin curve characterized by exponent  $b$ , which is optimized. We assume rapid particle dissolution (routinely modeled as instant, e.g., Najjar et al., 1992) and set  $k_{\text{poc}} = 1/\text{day}$ . The term  $U_{\text{C}}$  is the local photosynthetic uptake rate of dissolved inorganic carbon (DIC) per unit volume (organic carbon production rate).  $U_{\text{C}}$  is parameterized in terms of satellite-derived net primary productivity (NPP) and observed phosphate concentration (for details, see Holzer, Kwon, & Pasquier, 2021).  $\sigma$  is the fraction of the organic carbon production that immediately results in semilabile DOC without first passing through the POC pool.

The OUR is given by

$$\text{OUR} = R_{\text{O}_2:\text{C}} \kappa_{\text{doc}} \Theta ([\text{O}_2] - [\text{O}_2]_{\text{min}}) [\text{DOC}], \quad (2)$$

where  $R_{\text{O}_2:\text{C}}$  is the  $\text{O}_2:\text{C}$  stoichiometric ratio which is treated as an optimizable parameter,  $\kappa_{\text{doc}}^{-1}$  is the respiration timescale (also optimized), and  $\Theta$  is a step function preventing oxygen utilization in suboxic waters where  $[\text{O}_2] < [\text{O}_2]_{\text{min}}$ . We set  $[\text{O}_2]_{\text{min}} = 5 \mu\text{M}$  and to ensure differentiability we use the smooth step  $\Theta(x) = [1 + \tanh(x/x_0)]/2$ , with  $x_0 = 1 \mu\text{M}$  (corresponding to a hard cutoff around  $4 \mu\text{M}$  following Najjar et al. (2007)). The term  $R_{\text{O}_2:\text{C}} U_{\text{C}}$  represents the phytoplankton photosynthetic source of oxygen.

In Equation 1,  $K_{\text{as}}$  is the air-sea exchange coefficient for oxygen, and  $[\text{O}_2]_{\text{sat}}$  is the saturated equilibrium oxygen concentration calculated from the temperature and salinity dependent solubility (Wanninkhof, 1992) and a prescribed atmospheric oxygen partial pressure of 0.210 atm.  $K_{\text{as}}$  is given by  $K_{\text{as}} = K_w/\Delta z_1$  where  $\Delta z_1$  is the thickness of the model's surface layer, and the gas-exchange velocity  $K_w$  is parameterized as  $K_w = s_w a (1 - f_{\text{ice}}) U^2 (\text{Sc}/660)^{-1/2}$ , where  $U^2$  is the climatological squared surface wind speed,  $f_{\text{ice}}$  is the climatological sea-ice fraction, and  $a = 0.251 \text{ cm hr}^{-1} \text{ m}^{-2} \text{ s}^2$  (Wanninkhof et al., 2013), and  $s_w$  is a fine-tuning scale factor that was optimized to  $s_w = 1.2$ . Both  $U^2$  and  $f_{\text{ice}}$  were calculated as averages of 6-hourly National Centers for Environmental Prediction reanalyzes for the period 1948–2014 (Kalnay et al., 1996). As in the work of DeVries and Holzer (2019), we use 6-hourly rather than monthly averages for wind speed so that the climatological averages of  $U^2$  capture a degree of gustiness. The temperature-dependent  $\text{O}_2$  Schmidt number  $\text{Sc}$  was calculated using the empirical fits of Wanninkhof (1992).

Model parameters are optimized by jointly minimizing the volume-weighted quadratic mismatch of DIC, phosphate ( $\text{PO}_4$ ), total alkalinity (TA), and  $\text{O}_2$  with the observed gridded annual-mean fields, correcting DIC for anthropogenic carbon (Holzer, Kwon, & Pasquier, 2021). The gridded observed  $\text{PO}_4$  concentration was taken

from the World Ocean Atlas (Garcia et al., 2010). The gridded DIC, TA, and  $O_2$  fields, nominally for the year 2002, are from the Global Data Analysis Project Version 2 (GLODAP2, Olsen et al., 2016). The parameters  $b$ ,  $\sigma$ ,  $\kappa_{\text{doc}}$ , and  $R_{O_2:C}$  are approximated as globally uniform and jointly optimized with the other parameters of the carbon cycle. As for the parent carbon-cycle model (Holzer, Kwon, & Pasquier, 2021), we consider a “base state” corresponding to optimized respiration timescale  $\kappa_{\text{doc}}^{-1}$  and (unperturbed) biological production based on observed  $[PO_4]$  and satellite-derived NPP estimates from the Vertically Generalized Production Model (VGPM, Behrenfeld & Falkowski, 1997). To assess uncertainty we consider three additional optimized states. Because  $\kappa_{\text{doc}}$  is relatively poorly constrained by the observations used (Holzer, Kwon, & Pasquier, 2021), we also consider model solutions with  $\kappa_{\text{doc}}^{-1}$  specified at a fixed value of 1.2 years (Teng et al., 2014), and to investigate uncertainty in biological production, we additionally use production based on NPP from the Carbon-based Production Model-2 (CbPM, Westberry et al., 2008). Except for the overall magnitude of the sensitivities to local biological production perturbations, the geographic pattern of these sensitivities and all other oxygen diagnostics considered here turn out to be robust to both the choice of respiration timescale and NPP product when other parameters are optimized. We therefore plot only fields for the base state. Uncertainties for numerical values quoted in the main text correspond to the half-range spread across our four optimized model states, which is dominated by the differences in  $\kappa_{\text{doc}}$ . Details on cost function choice, parameter values, and model fidelity to observations are provided in Appendix A.

## 2.2. Linear Oxygen Labeling Tracers

In order to trace oxygen through the nonlinear respiration process (2), we use a linear labeling tracer (for other applications of labeling tracers, see Holzer, Kwon, & Pasquier, 2021; Holzer et al., 2014; Pasquier & Holzer, 2016, 2018). We can think of these labels as attached to the oxygen molecules so that their concentration  $\chi = [O_2]$ . However, the labeling tracers participate in respiration and air-sea exchange in proportion to their concentration and thus obey an equation linear in  $\chi$ , allowing us to apply detailed transport diagnostics to oxygen. There is no need to introduce separate labeling tracers for DOC and POC because their equations are already linear.

We discretize all differential operators and fields on the numerical grid of OCIM2. With  $N \sim 2 \times 10^5$  ocean grid points, the operators  $\mathcal{T}$  and  $\mathcal{T}_{\text{poc}}$  become the sparse  $N \times N$  transport matrices  $\mathbf{T}$  and  $\mathbf{T}_{\text{poc}}$ , and the three-dimensional fields become  $N \times 1$  column vectors. Multiplication by the air-sea exchange coefficients becomes multiplication by the diagonal matrix  $\mathbf{K} \equiv \text{diag}(K_{\text{as}})$ . The key step for obtaining the equation for the labeling tracer concentration  $\chi$  is replacing the nonlinear OUR term with loss coefficients that simply multiply  $\chi$ . We diagnose these loss coefficients from the full nonlinear solution as the ratio  $\gamma \equiv \text{OUR}/[O_2]$  so that  $\text{OUR} = \mathbf{L} \chi$ , where  $\mathbf{L} = \text{diag}(\gamma)$ . The equation for the labeling tracer concentration  $\chi$  thus becomes

$$\partial_t \chi + \mathbf{A} \chi = S_{\text{atm}} + S_{\text{bio}}, \quad (3)$$

where  $\mathbf{A} = \mathbf{T} + \mathbf{K} + \mathbf{L}$  and  $S_{\text{atm}} \equiv \mathbf{K} [O_2]^{\text{sat}}$  is the source term due to the one-way atmosphere-to-ocean flux of oxygen, while  $S_{\text{bio}} \equiv R_{O_2:C} U_C$  is the oxygen source from phytoplankton photosynthesis. Note that the linear Equation 3 has by construction exactly the same solution as the non-linear oxygen model, that is,  $\chi = [O_2]$ . We use (3) below to partition the oxygen concentration in various ways. For example, the steady-state photosynthetic and atmosphere-injected oxygen concentrations are readily obtained as  $[O_2]^{\text{bio}} = \mathbf{A}^{-1} S_{\text{bio}}$  and  $[O_2]^{\text{atm}} = \mathbf{A}^{-1} S_{\text{atm}}$ , with  $[O_2]^{\text{bio}} + [O_2]^{\text{atm}} = [O_2]$ .

## 3. Results

### 3.1. Oxygen Distribution and Definition of Low-Oxygen Regions

Key fields of the model oxygen cycle are shown in Figure 1 as Pacific zonal means. The model fits the oxygen observations overall quite well with a global root-mean-square misfit of only  $20 \mu\text{M}$  (see also the binned, volume-weighted scatter plot of model vs. observed oxygen concentrations in Appendix Figure A1). However, despite parameter optimization, Figure 1 shows that there are also some systematic biases in the modeled oxygen. In terms of the Pacific zonal mean  $[O_2]$  (Figures 1a and 1b), the oxygen-deficient region of the North Pacific is vertically too thick at low latitudes and not thick enough (and slightly too oxygen rich) at high northern latitudes. Relatedly, the  $[O_2]$  contours in the deep North Pacific do not slope down as much with increasing latitude as seen

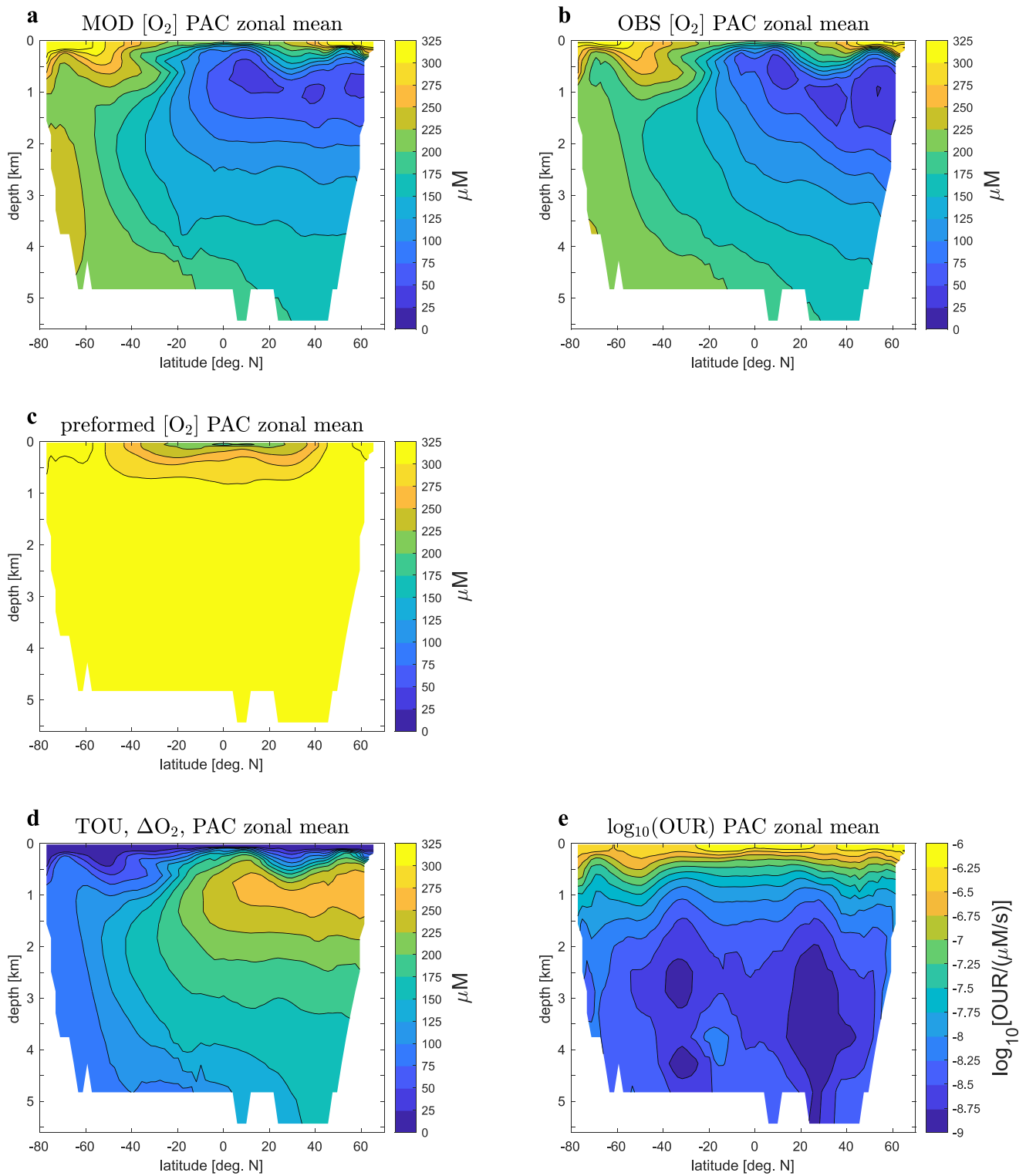


**Figure 1.** Pacific zonal means of the modeled (a) and observed (b) oxygen concentrations, as well as of the modeled preformed oxygen concentration (c), true oxygen utilization (TOU) (d), and oxygen utilization rate (OUR) (e). (Note the logarithmic color scale for OUR).

in the observations. Below the thermocline, preformed oxygen concentrations  $[O_2]_{pre}$  (Figure 1c) are an approximately uniform admixture of the high-latitude endmembers where solubility is high in cold waters. The resulting TOU (Figure 1d), defined as  $\Delta O_2 \equiv [O_2]_{pre} - [O_2]$ , is correspondingly largely a mirror image of  $[O_2]$  at depth. The OUR (Figure 1e—note the logarithmic scale) is essentially proportional to the semilabile DOC concentration (cf. Equation (2)) and hence decays rapidly with depth and features minima below the oligotrophic subtropical gyres. Our model estimates that only  $(5 \pm 1)\%$  of the total oxygen content is photosynthesized in the ocean.

We consider three interior regions of the ocean for which we examine the sensitivity of the oxygen content to perturbations in biological production. One region is the global ocean, and two are low-oxygen regions of the Pacific defined by  $[O_2]$  lying below specified thresholds. We denote both a given region and its mask vector (unity for points in the region, zero elsewhere) by  $\Omega$ . Because the volume and shape of the low-oxygen regions are sensitive to the value of the  $[O_2]$  threshold used to define them, the biases of the model require that different thresholds be used for model and observations to map out comparable regions of equivalent volume. We thus define the NP OMZ as the region of the North Pacific for which  $[O_2] < 20 \mu\text{M}$  for the observations and  $[O_2] < 29.0 \pm 0.7 \mu\text{M}$  for the model. While OMZ's have received much attention because they contain suboxic regions of importance to the global nitrogen cycle, a much larger volume of the Pacific has hypoxic conditions. The hypoxic limit for marine life is widely considered to be  $2 \text{ mg } O_2/\ell$  but even twice that concentration has been shown to be lethally low for many benthic species (Vaquer-Sunyer & Duarte, 2008). Here we define the Pacific Hypoxic Zone (PHZ) as the part of the Pacific for which  $[O_2] < 62.5 \mu\text{M}$  (equivalent to  $2 \text{ mg } O_2/\ell$ ) for the observations, which is matched in volume by the model if  $[O_2] < 66.3 \pm 0.4 \mu\text{M}$ . To ensure the regions are as comparable as possible to their observational counterparts, we additionally limited both the modeled and observed NP OMZ to lie between  $3^\circ\text{N}$  and  $31^\circ\text{N}$ , and the PHZ to lie east of  $140^\circ\text{E}$ . Figure 2 shows that while there are differences between model and observations, the overall shape and character of these regions is reasonably approximated by the model. The chief difference between model and observations is that the modeled PHZ is vertically several hundred meters less thick at high northern latitudes, and in the horizontal lacks the pronounced equatorial minimum seen in the observations. However, the concentration thresholds needed to give the modeled and observed PHZ the same volume differ by only about 6%.

It is important to appreciate that the shape of low-oxygen zones is by its very nature sensitive to small changes in the oxygen concentration and well-known to be difficult to model. For example, a comparison of the Pacific OMZ with  $[O_2] \leq 30 \mu\text{M}$  across CMIP5 models (Cabr e et al., 2015), shows that none of these models managed to capture the observed shape of the  $30\mu\text{M}$  oxygen isosurface and there is a very large spread across models in both the vertical and horizontal structure of the modeled OMZ. The mismatch between CMIP5 models and observations is particularly striking at 1,000 m depth in the northern extratropical Pacific. For our purposes here, however, the modeled oxygen field's dynamical consistency with the circulation and biogeochemistry is much more important than the detailed realism of the PHZ. As shown below, our simple model is more than adequate for demonstrating the nature of a given region's sensitivity to production changes, for mapping out the origin of its oxygen deficit, and for illustrating the link with the associated newly developed transport timescales.

### 3.2. Sensitivity to Local Changes in Biological Production

We calculate the sensitivity of the oxygen system to a small-amplitude perturbation  $\delta U_C(\mathbf{r}_e)$  in biological production at location  $\mathbf{r}_e$  in the euphotic zone. To do this efficiently for every grid point  $\mathbf{r}_e$ , we employ an adjoint technique as detailed in Appendix B1. This analysis provides the  $\Omega$ -integrated response  $\delta q(\mathbf{r}_e)$  of the quantity of interest (we focus on TOU or  $[O_2]$  here), per perturbation-grid-box volume. Because  $\delta q(\mathbf{r}_e)$  is proportional to  $\delta U_C(\mathbf{r}_e)$ , we consider the vertically integrated response per unit vertically integrated production change, that is, we consider the sensitivity maps defined by

$$S \equiv \frac{\int \delta q dz}{\int \delta U_C dz}, \quad (4)$$

where the integrands are non-zero only in the euphotic zone (top 2 layers for our model).

Figure 3 shows the sensitivity of the  $\Omega$ -integrated TOU, which except for a change in sign is very similar to the corresponding sensitivity of the  $\Omega$ -integrated oxygen content (red curves in Figures 3b, 3d and 3f). Because the magnitude of the OUR field is sensitive to the relatively uncertain value of the inverse respiration timescale  $\kappa_{doc}$

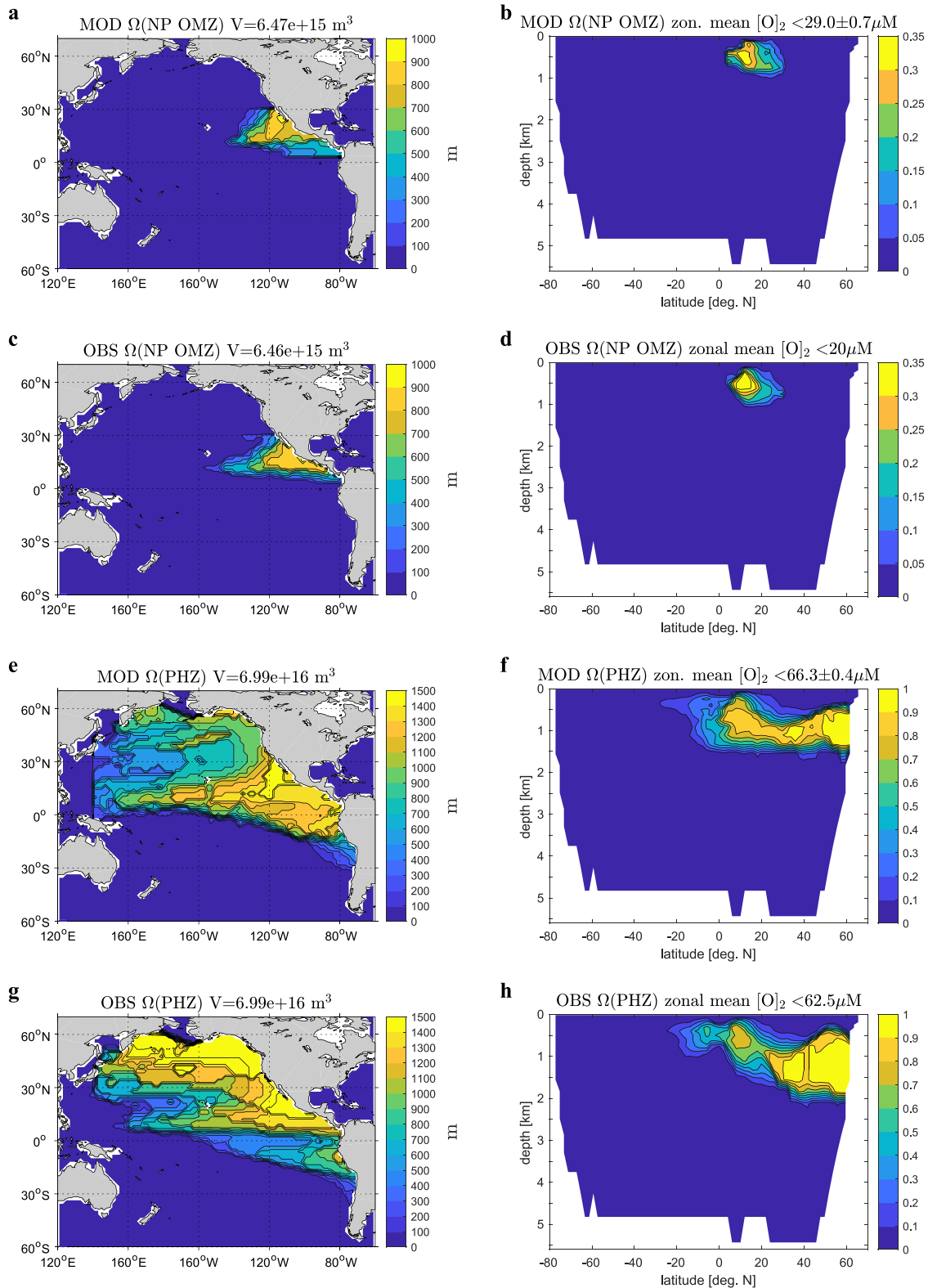


**Figure 2.** Vertical integrals (left) and Pacific zonal means (right) of the masks of the low-oxygen regions  $\Omega$  defined for the modeled oxygen field (a, b, e, f) and for the observed oxygen field (c, d, g, h). The titles on the left include the volume  $V$  of  $\Omega$ , and the titles on the right include the corresponding concentration threshold that was used to define the masks. Note that to compensate for model bias, different thresholds were used for model and observations to match the volumes of the regions. Plots a–d show the North Pacific oxygen minimum zone (NP OMZ), while plots e–h show the Pacific Hypoxic Zone (PHZ).

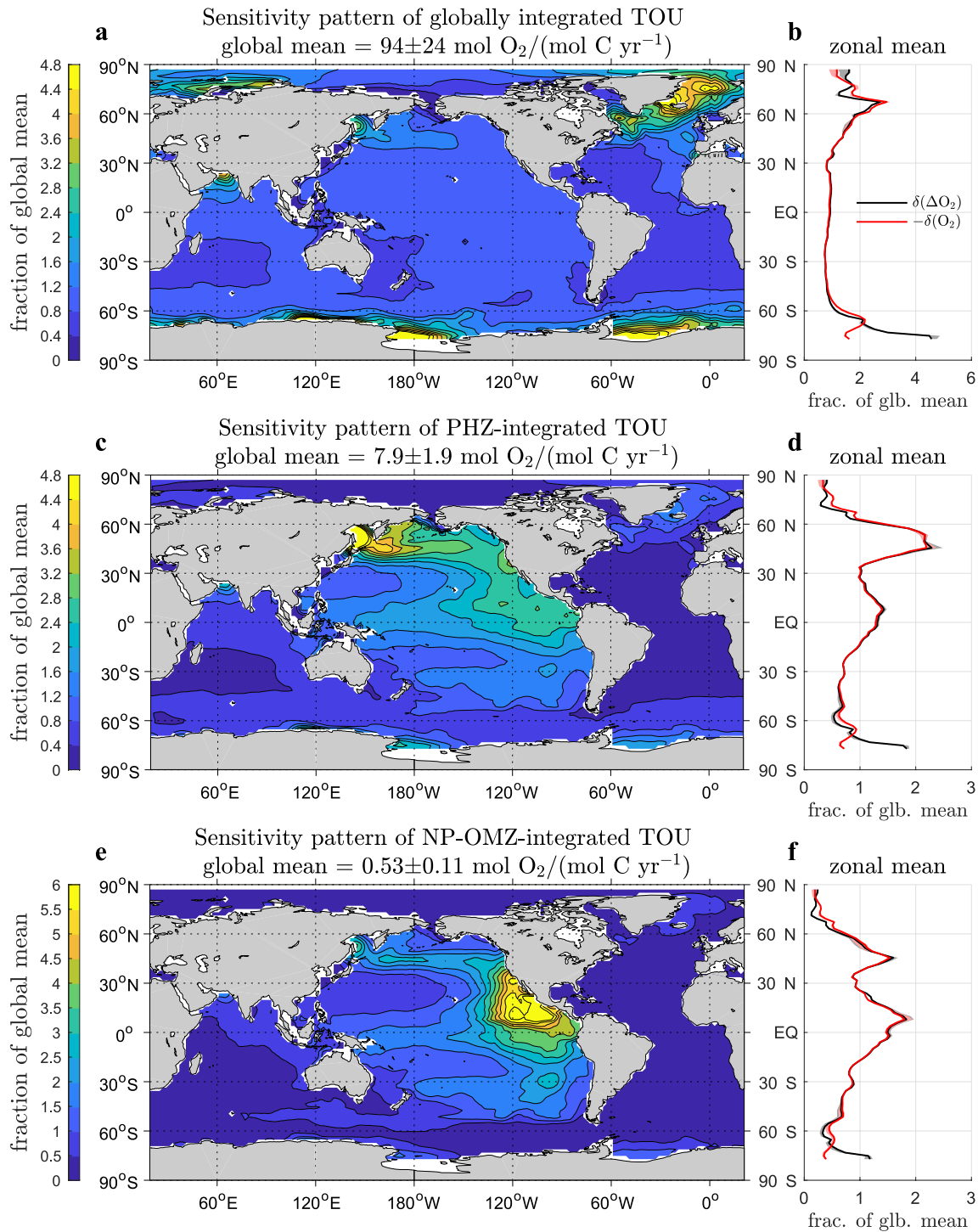


**Figure 3.** Patterns of the sensitivity of the  $\Omega$ -integrated true oxygen utilization (TOU) to point-wise perturbations in biological production, for  $\Omega$  being the global ocean (a, b), the Pacific Hypoxic Zone (PHZ, c, d), and the North Pacific oxygen minimum zone (NP OMZ) (e, f). These patterns are the sensitivity maps  $S$  of Equation 4 normalized by their global ocean mean; parts a,c,e show the normalized maps and parts b,d,f show the corresponding global zonal means. The zonal means show the sensitivities of both the  $\Omega$ -integrated TOU (black) and the  $\Omega$ -integrated oxygen content (red). Note that for the oxygen content, the negative of the sensitivity has been plotted as increased production decreases the overall oxygen content. The shading of the zonal means shows their spread for a factor of  $\sim 3$  change in respiration timescale, with other parameters optimized.



(but not simply proportional to it as the optimization of other parameters also changes the amount of production routed to semilabile DOC, thus partially compensating), we focus in Figure 3 on the *patterns* of the sensitivity map, that is, on  $S$  normalized by its global mean. These patterns are not sensitive to the choice of optimized state as can be seen from the small spread in their zonal means (Figures 3b, 3d and 3f) for a roughly threefold range in respiration timescale. The sensitivities for TOU and  $O_2$  content, whether normalized or not, are very similar and differ most in Antarctic marginal seas where the TOU sensitivity is larger (Figures 3b, 3d and 3f). The reason for this lies in the opposing responses of photosynthetic oxygen  $[O_2]^{bio}$  and atmosphere-sourced oxygen  $[O_2]^{atm}$  (calculated separately but not shown): For Antarctic marginal seas and the bottom-waters sources there,  $[O_2]^{bio}$  makes about a 10% contribution near the surface and  $\sim 5\%$  in the abyss, with  $[O_2]^{atm}$  being correspondingly lower, presumably because of the poor air-sea exchange in these largely ice-covered seas. Increasing biological production increases  $[O_2]^{bio}$  while at the same time decreasing  $[O_2]^{atm}$  by increasing DOC and utilization, with these opposing effects largely canceling in the response of the interior oxygen content. For  $\Delta O_2 = [O_2]_{pre} - [O_2]$  increased photosynthetic oxygen increases both  $[O_2]_{pre}$  and  $[O_2]$  so that the difference  $\Delta O_2$  is largely unaffected by increased photosynthesis. However, increased production increases respiration (through increased [DOC]), so that  $\Delta O_2$  increases, which leads to increased TOU sensitivity as there is no counteracting photosynthetic effect.

Geographically, the sensitivity pattern of the globally integrated TOU (Figure 3a) is dominated by the world ocean's deep-water formation regions (northern Atlantic, Weddel Sea, Ross Sea). Increasing production and hence OUR in these regions strips oxygen out of cold, high-solubility waters entering the deep interior. The pattern for the PHZ-integrated TOU (Figure 3c) still shows some sensitivity in the deep-water formation regions, but the main sensitivity now lies in the midlatitude mode/intermediate-water formation regions of the North and South Pacific and in the tropical eastern Pacific. The sensitivity pattern for the NP OMZ (Figure 3e) has a similar structure, but with a more dominant contribution from immediately above the NP OMZ.

The patterns of Figure 3 show that the sensitivity is high where (i) the water in the interior regions was last ventilated, with increased organic-matter respiration in these areas stripping oxygen out of the source waters, and where (ii) a stimulated biological pump can directly inject increased organic matter into the interior volumes fueling their respiration. The amplitude of the sensitivities  $S$  (quantified by their global mean—see titles in Figures 3a, 3c and 3e) scales approximately with the volume of  $\Omega$  and has a half-range uncertainty of about 25% for our roughly threefold range in respiration timescale  $\kappa_{doc}^{-1}$ . Below we will examine in detail where the oxygen loss occurs that leads to the  $\Omega$ -integrated TOU, and how the interplay between the biological pump and the circulation controls the TOU sensitivity pattern.

### 3.3. Controls on the TOU Sensitivity to Production Changes

#### 3.3.1. Surface Oxygen Flux

We first consider the atmosphere-to-ocean flux of oxygen that is destined to be utilized in a given region  $\Omega$ . The amount of oxygen utilized in  $\Omega$  per unit time due to each grid box of atmospheric injection source  $S_A$  is given from Equation 3 by  $w^T \mathbf{L} \Omega \mathbf{A}^{-1} \mathbf{diag}(S_A)$ , where  $w$  is the column vector of grid-box volumes and  $\Omega \equiv \mathbf{diag}(\Omega)$  is the matrix operator masking out region  $\Omega$ . (Superscript  $T$  denotes matrix transpose.) For efficient computation, we take the transpose and divide by the surface area  $a$  of each grid box to obtain the flux of oxygen into the ocean that is destined to be utilized in  $\Omega$  as  $\Phi = \mathbf{diag}^{-1}(a) \mathbf{diag}(S_A) \mathbf{W} \tilde{\mathbf{A}}^{-1} \mathbf{L} \Omega$ , where  $\mathbf{W} \equiv \mathbf{diag}(w)$  and  $\tilde{\mathbf{A}} \equiv \mathbf{W}^{-1} \mathbf{A}^T \mathbf{W}$  is the adjoint of  $\mathbf{A}$  with respect to the volume-weighted inner product.

Figure 4 shows  $\Phi$  normalized by the  $\Omega$ -integrated utilization rate on a logarithmic scale for the three  $\Omega$  regions considered. The geographic pattern of the flux of oxygen destined to be utilized anywhere (i.e.,  $\Omega$  is the global ocean, Figure 4a) is set by the pattern of water-mass ventilation modulated by the pattern of the air-sea exchange coefficients. The oxygen fluxes supplying utilization in the PHZ (Figure 4b) and in the NP OMZ (Figure 4c) have similar patterns that emphasize the mode and intermediate water formation regions of the Pacific. North Atlantic and Antarctic deep-water formation regions are more important for the deeper and more extensive PHZ than for the shallower and smaller NP OMZ. Figures 4b and 4c shows that the midlatitude high-sensitivity regions in the Pacific are also regions of high oxygen supply, with sensitivity being high because increased organic-matter production can strip oxygen out of the supply. However, the pattern of the oxygen flux and that of the sensitivity

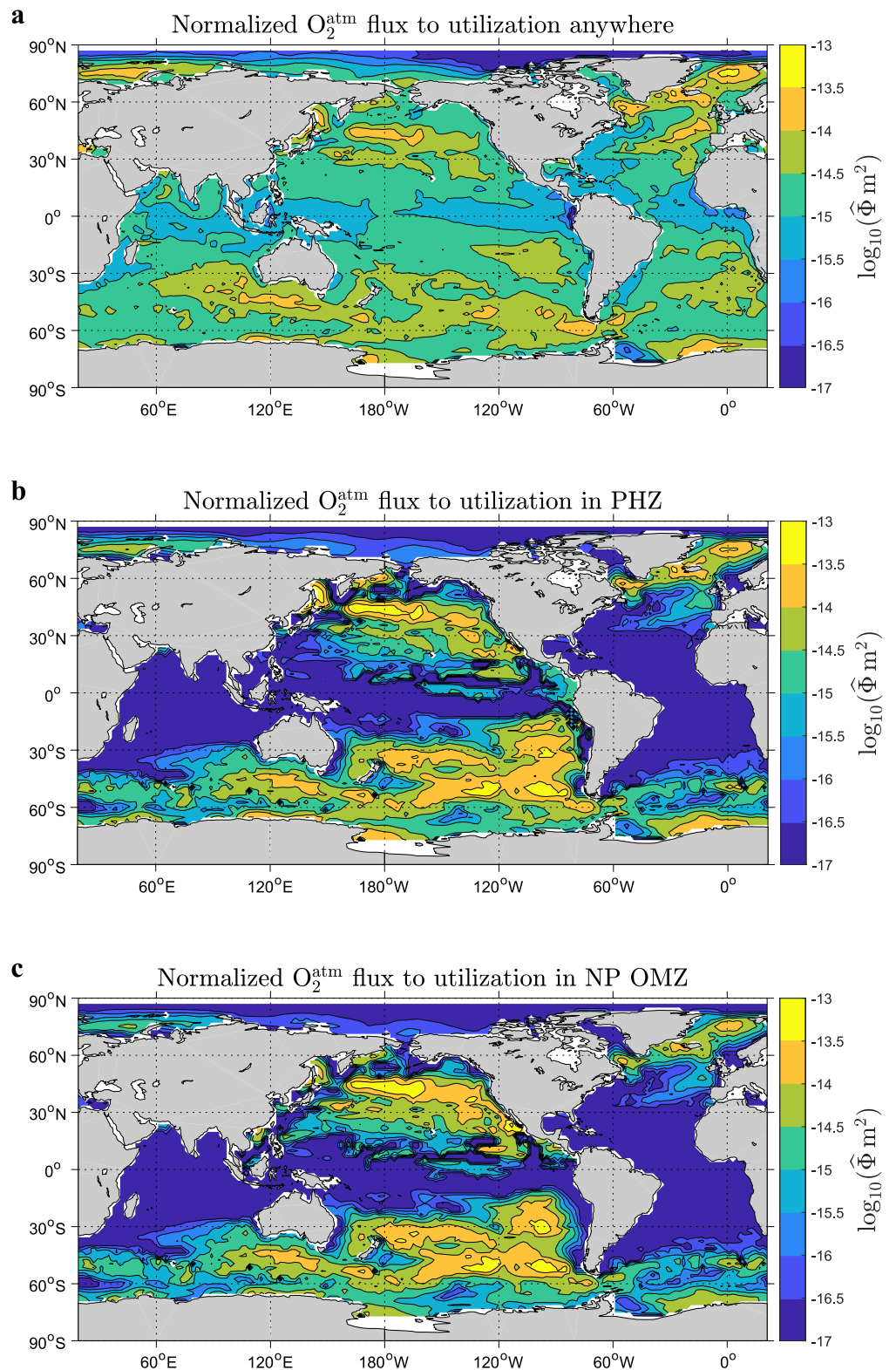


**Figure 4.** The flux of  $O_2$  from the atmosphere into the ocean that is destined to be utilized in region  $\Omega$ , with  $\Omega$  being the global ocean (a), the Pacific Hypoxic Zone (PHZ, b), and the North Pacific oxygen minimum zone (NP OMZ) (c). Because these fluxes depend on the size and location of  $\Omega$ , they have been normalized by their global integral for plotting. Note the logarithmic color scale, that is, the plots show the logarithm of  $\hat{\Phi} \equiv \Phi / \int \Phi d^2r$  in units of  $\text{m}^{-2}$ .

are not strongly correlated as the atmosphere-to- $\Omega$  oxygen flux cannot capture the effects of increased DOC injection into poorly ventilated regions such as  $\Omega$  itself.

An analogous analysis shows that flow rate of photosynthetic oxygen, from production to utilization anywhere, is only around 3% of the corresponding flow rate of atmospheric oxygen. In terms of pattern (not shown) there are differences in coastal regions, but the open-ocean pattern is similar to that for atmospheric oxygen. To better understand what sets the sensitivity to biological changes, we now investigate where the oxygen utilization occurs that leads to the oxygen deficit of  $\Omega$ .

### 3.3.2. Where Does the $\Omega$ -Integrated Oxygen Deficit Originate?

The TOU in region  $\Omega$  represents an oxygen deficit compared to the preformed oxygen concentration and is due to utilization both within  $\Omega$  and upstream from  $\Omega$ . To find out where the utilization occurred that causes the oxygen deficit of  $\Omega$ , we first develop the equation for TOU (Ito et al., 2004) defined as  $\Delta O_2 \equiv [O_2]_{\text{pre}} - [O_2]$ . The preformed oxygen concentration  $[O_2]_{\text{pre}}$  can be considered to be the tracer response to clamping the surface oxygen concentration to that of the full solution but without any interior sinks or sources. The simplest way to enforce this boundary condition is via fast relaxation with a suitable timescale  $\tau$ . (For sufficiently short  $\tau$  there is no sensitivity to its precise value—we use  $\tau = 10$  s; because the euphotic zone lies within the mixed layer it also makes virtually no difference if the top layer or the euphotic zone are used.) Denoting the mask vector for the euphotic zone by  $\Omega_{\text{eu}}$  and defining the diagonal linear operator  $\mathbf{L}_a \equiv \text{diag}(\Omega_{\text{eu}}/\tau)$ , preformed oxygen thus obeys  $\mathbf{T} [O_2]_{\text{pre}} = \mathbf{L}_a ([O_2]^* - [O_2]_{\text{pre}})$ , where the \* superscript reminds us that this is the prescribed oxygen field. We can similarly consider the actual oxygen field to be the solution of the oxygen equation when the euphotic concentrations are also prescribed via fast relaxation. These prescribed surface boundary conditions replace the air-sea exchange terms, but unlike for  $[O_2]_{\text{pre}}$ , interior utilization does act on the full  $[O_2]$  concentration so that  $\mathbf{T} [O_2] = \mathbf{L}_a ([O_2]^* - [O_2]) - \text{OUR}$ . Taking the difference of these equations, we obtain the equation for the TOU,  $\Delta O_2$ :

$$\mathbf{T}_a \Delta O_2 = \text{OUR}, \quad (5)$$

where  $\mathbf{T}_a \equiv \mathbf{T} + \mathbf{L}_a$ . Thus,  $\Delta O_2$  can be considered to be the tracer response to the OUR sink field, mediated by advective-diffusive water transport alone, with a boundary condition of  $\Delta O_2 = 0$  in the euphotic layer (enforced by  $\mathbf{L}_a$ ).

The response field due to the OUR of a given single grid box can now be obtained by simply zeroing OUR in all other grid boxes. Organizing the column vectors of such responses to single-grid-box OUR from each grid box into matrix  $\Delta \mathbf{O}_2$ , we obtain  $\Delta \mathbf{O}_2 = \mathbf{T}_a^{-1} \text{diag}(\text{OUR})$ , as each column of  $\text{diag}(\text{OUR})$  corresponds to the OUR of the single grid box at the location of the diagonal entry. To collapse the information from  $\sim 2 \times 10^5$  response fields, we volume integrate over  $\Omega$ . We thus consider  $u^T \Omega \Delta \mathbf{O}_2$  and multiply from the right by  $\mathbf{W}^{-1}$  to obtain the  $\Omega$ -integrated response per unit volume of the grid box where the utilization took place. Taking the transpose for efficient computation gives the contribution per unit volume from each grid point  $\mathbf{r}$  in the ocean to the  $\Omega$ -integrated oxygen deficit, which we denote by  $\Delta O_2(\mathbf{r} \rightarrow \Omega)$ :

$$\begin{aligned} \Delta O_2(\mathbf{r} \rightarrow \Omega) &= \text{diag}(\text{OUR}) \tilde{\mathbf{T}}_a^{-1} \Omega \\ &= \text{OUR}(\mathbf{r}) \Gamma_{\Omega}^1(\mathbf{r}), \end{aligned} \quad (6)$$

where  $\tilde{\mathbf{T}}_a \equiv \mathbf{W}^{-1} \mathbf{T}_a^T \mathbf{W}$  is the adjoint transport operator, which is the transport operator of the time-reversed adjoint flow. Note that  $\tilde{\mathbf{T}}_a^{-1}$  can be thought of as tracing water in  $\Omega$  back in time. Thus,  $\Delta O_2(\mathbf{r} \rightarrow \Omega)$  partitions the  $\Omega$ -integrated TOU according to where it originated through respiration in the past, that is,

$$\int_{\text{ocean}} \Delta O_2(\mathbf{r} \rightarrow \Omega) d^3 r = \int_{\Omega} \Delta O_2 d^3 r, \quad (7)$$

where we have used continuous notation for the volume integrals (volume element  $d^3 r$ ).

The last equality of Equation 6 recognizes that  $\Gamma_{\Omega}^1 = \tilde{\mathbf{T}}_a^{-1} \Omega$  is the mean water re-exposure time spent in region  $\Omega$ . Specifically, if  $\Omega$  is the global ocean volume, then  $\Gamma_{\Omega}^1(\mathbf{r})$  is simply the mean transit time (or re-exposure time) for fluid elements at point  $\mathbf{r}$  to make their *next* contact with the surface layer  $\Omega_{\text{eu}}$ . This re-exposure time has been discussed in the literature (Primeau, 2005; DeVries & Primeau, 2011; DeVries & Holzer, 2019; Holzer, DeVries,

& de Lavergne, 2021), and its zonal mean for OCIM2 is shown in Appendix D for reference. If  $\Omega$  is a subregion of the ocean, then  $\Gamma_{\Omega}^{\uparrow}(\mathbf{r})$  is the mean time that water spends in  $\Omega$  on its way from point  $\mathbf{r}$  to next contact with  $\Omega_{\text{eu}}$  as derived in Appendix D.

Equation 6 shows that it is the mean re-exposure time  $\Gamma_{\Omega}^{\uparrow}$  and *not* the mean age that connects the TOU in volume  $\Omega$  to the respiration encountered on the way to  $\Omega$ . In interpreting the patterns of  $\Delta O_2(\mathbf{r} \rightarrow \Omega)$  it is useful to think of  $\Gamma_{\Omega}^{\uparrow}$  at point  $\mathbf{r}$  as a kind of path selector: In order for the OUR at  $\mathbf{r}$  to contribute significantly to the oxygen deficit of  $\Omega$ , the transport paths of water carrying oxygen from  $\mathbf{r}$  to the surface must pass through  $\Omega$  and spend as much time there as possible. In steady state, the re-exposure time accumulated in  $\Omega$  is equal to the time for which the oxygen is swept past  $\mathbf{r}$  and hence it is  $\text{OUR}(\mathbf{r})$  acting for this time that determines how much of the oxygen deficit of  $\Omega$  originated at  $\mathbf{r}$ .

Figure 5 shows the spatial distribution of  $\Delta O_2(\mathbf{r} \rightarrow \Omega)$  in terms of maps of vertical integrals, Pacific zonal means, and vertical profiles. The maps show that there is a close correspondence between  $\Delta O_2(\mathbf{r} \rightarrow \Omega)$  and the sensitivity maps of Figure 3. For the global-ocean case (Figure 5a) the Antarctic and North Atlantic deep-water formation regions feature as prominent locations of oxygen loss, while for the PHZ and NP OMZ (Figures 5d and 5g),  $\Delta O_2(\mathbf{r} \rightarrow \Omega)$  has the same three-pronged pattern as the TOU sensitivity, with high oxygen loss at mid latitudes and in the eastern tropical Pacific. While the largest oxygen loss occurs in the upper ocean (Figures 5b, 5e and 5h), the globally integrated TOU also has significant benthic/abyssal contributions (Figure 5b), with  $17.7 \pm 0.3\%$  of the globally integrated TOU being due to respiration below 3,068 m depth. Using Equation 6, we find that OUR dominates the vertical structure of  $\Delta O_2(\mathbf{r} \rightarrow \Omega)$  by weighting the  $\Gamma_{\Omega}^{\uparrow}$  toward the upper ocean, while the horizontal structure of  $\Delta O_2(\mathbf{r} \rightarrow \Omega)$  is dominated by the distribution of  $\Gamma_{\Omega}^{\uparrow}$ .

### 3.3.3. Mean Re-Exposure Time Spent in $\Omega$ Links TOU Sensitivity and OUR

We can now see how  $\Gamma_{\Omega}^{\uparrow}$ , the mean re-exposure time that was spent in  $\Omega$ , combines with the OUR field to shape the TOU sensitivity maps. From Equations 6 and 7 it follows that the response of the  $\Omega$ -integrated TOU to a localized production perturbation is given by  $\int_{\Omega} \delta(\Delta O_2) d^3r = \int_{\text{ocean}} \Gamma_{\Omega}^{\uparrow}(\mathbf{r}) \delta \text{OUR}(\mathbf{r}) d^3r$ , where we used  $\delta \Gamma_{\Omega}^{\uparrow} = 0$  because the ocean circulation is kept unperturbed. As shown in Appendix B2, this integral of  $\delta \text{OUR}$  can be approximated in terms of the unperturbed OUR field itself resulting in the approximate relation

$$S_{\text{TOU}} \approx R_{O_2-C} \frac{\int \Gamma_{\Omega}^{\uparrow} \text{OUR} dz}{\int \text{OUR} dz}. \quad (8)$$

The main approximation leading to (8) is that the plume of the semilabile DOC response stays beneath where the production is perturbed until it is respired. The approximate sensitivities on the right-hand-side of Equation 8 have a qualitatively similar large-scale pattern as the actual sensitivities of Figure 3, but overestimate the sensitivity in the most sensitive regions. Nevertheless, the linear correlation coefficients between actual and approximate sensitivity patterns are  $0.75 \pm 0.04$ ,  $0.906 \pm 0.008$ , and  $0.945 \pm 0.002$  for  $\Omega$  being the global ocean, PHZ, and NP OMZ, respectively. Approximation (8) demonstrates that the key control on the TOU sensitivity maps is the mean re-exposure time  $\Gamma_{\Omega}^{\uparrow}$  (accumulated in  $\Omega$ ) vertically averaged with the climatological OUR.

## 3.4. Fate of Oxygen

We now consider the fate of oxygen in the ocean more broadly by asking (a) where the oxygen in  $\Omega$  will be utilized, and (b) how much of the oxygen at any given point in the ocean will be utilized in  $\Omega$ .

### 3.4.1. Where Will the Oxygen Currently in $\Omega$ Be Utilized?

To answer this question, we use our linear labeling tracers to track the oxygen distribution currently in  $\Omega$ , denoted by  $\chi_{\Omega}$ , to where it will be utilized. The future time evolution of  $\chi_{\Omega}$  is governed by the initial value problem

$$\partial_t \chi_{\Omega} + \mathbf{A} \chi_{\Omega} = \mathbf{\Omega} [O_2] \delta(t), \quad (9)$$

where  $\mathbf{A} \equiv \mathbf{T} + \mathbf{L} + \mathbf{K}$  as in Equation 3 and  $\delta(t)$  is a Dirac  $\delta$ -function. The local loss rate per unit volume of this time-evolving oxygen plume is given by  $\mathbf{L} \chi_{\Omega}$  and the total oxygen that started from  $\Omega$  at  $t = 0$  that is lost at a given point  $\mathbf{r}$  per unit volume is given by the time integral of this rate, which we denote by  $O_2^{\uparrow}(\Omega \rightarrow \mathbf{r}) \equiv \int_0^{\infty} \mathbf{L} \chi_{\Omega} dt$ ,

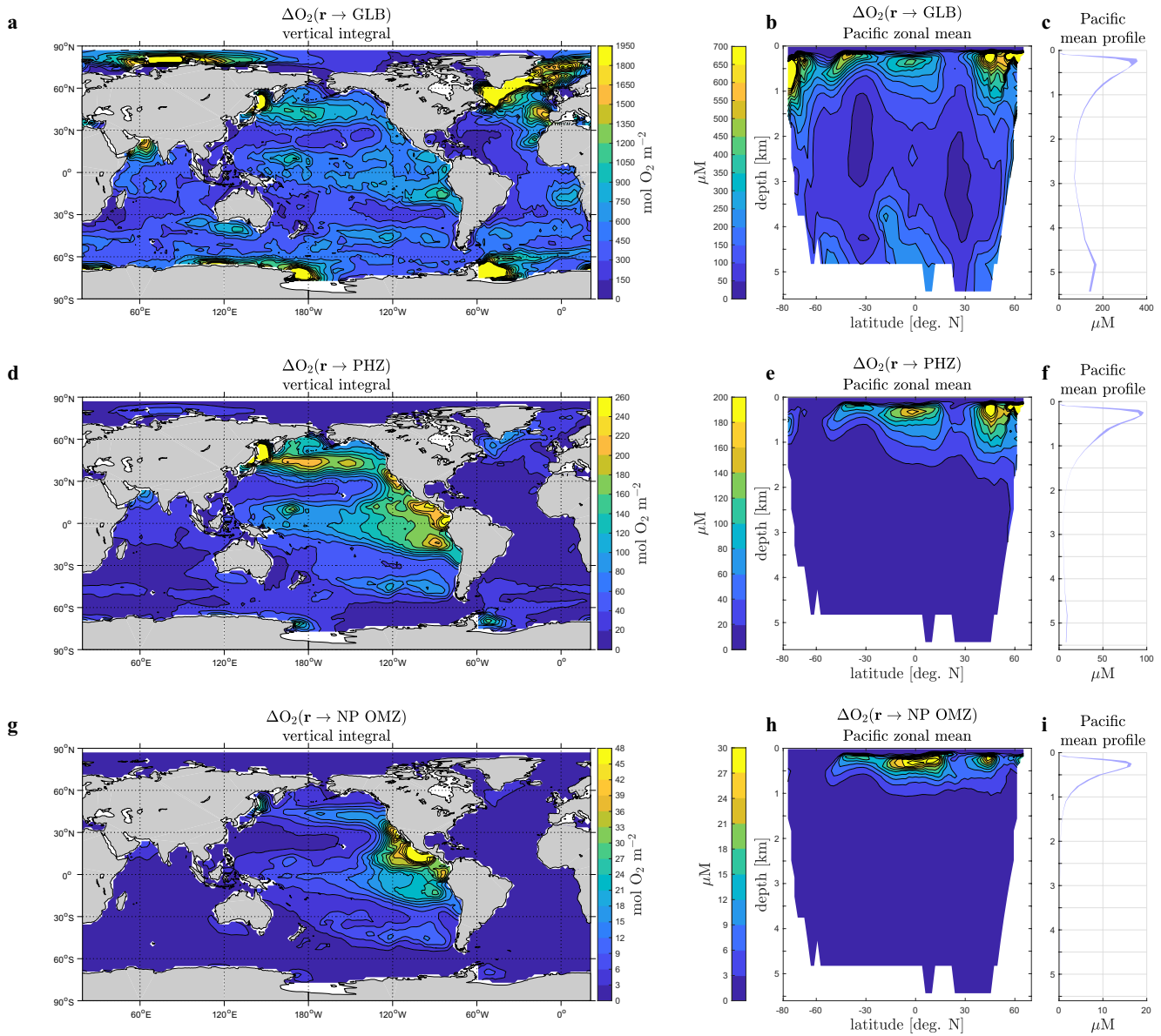


**Figure 5.** The local contributions  $\Delta O_2(\mathbf{r} \rightarrow \Omega)$  at point  $\mathbf{r}$  to the  $\Omega$ -integrated oxygen deficit due to respiration at  $\mathbf{r}$ . The vertical integrals (left), Pacific zonal means (middle), and Pacific mean vertical profiles (right) are shown for the three  $\Omega$  regions considered: The global ocean (a, b, c), the Pacific Hypoxic Zone (PHZ, d, e, f), and the North Pacific oxygen minimum zone (OMZ) (g, h, i). The shading of the profiles shows their spread for a factor or  $\sim 3$  change in respiration timescale, with other parameters optimized.

with the superscript  $\uparrow$  signifying loss. One readily obtains that the oxygen currently in  $\Omega$  that is lost per unit volume at point  $\mathbf{r}$  is given by

$$\begin{aligned}
 O_2^\uparrow(\Omega \rightarrow \mathbf{r}) &= \mathbf{L} \mathbf{A}^{-1} \mathbf{\Omega} [O_2] \\
 &= \mathbf{L} \mathbf{diag}([O_2]) \mathbf{diag}^{-1}([O_2]) \mathbf{A}^{-1} \mathbf{\Omega} [O_2] \\
 &= \text{OUR}(\mathbf{r}) \Gamma_{\text{ox}, \Omega}^\downarrow(\mathbf{r}),
 \end{aligned} \tag{10}$$

where the last equality follows from the fact that  $\text{OUR} = \mathbf{L} [O_2]$  and  $\mathbf{diag}^{-1}([O_2]) \mathbf{A}^{-1} \mathbf{\Omega} [O_2] = \Gamma_{\text{ox}, \Omega}^\downarrow$  is the mean oxygen age (since “birth” by atmospheric injection and photosynthesis) that is accumulated in  $\Omega$  as derived in Appendix D. (Note that in 10, the expression  $\mathbf{A}^{-1} \mathbf{\Omega} [O_2]$  can be thought of as propagating the oxygen concentration in  $\Omega$  forward in time.) The timescale  $\Gamma_{\text{ox}, \Omega}^\downarrow(\mathbf{r})$  is again a selector of paths, in this case paths of oxygen from

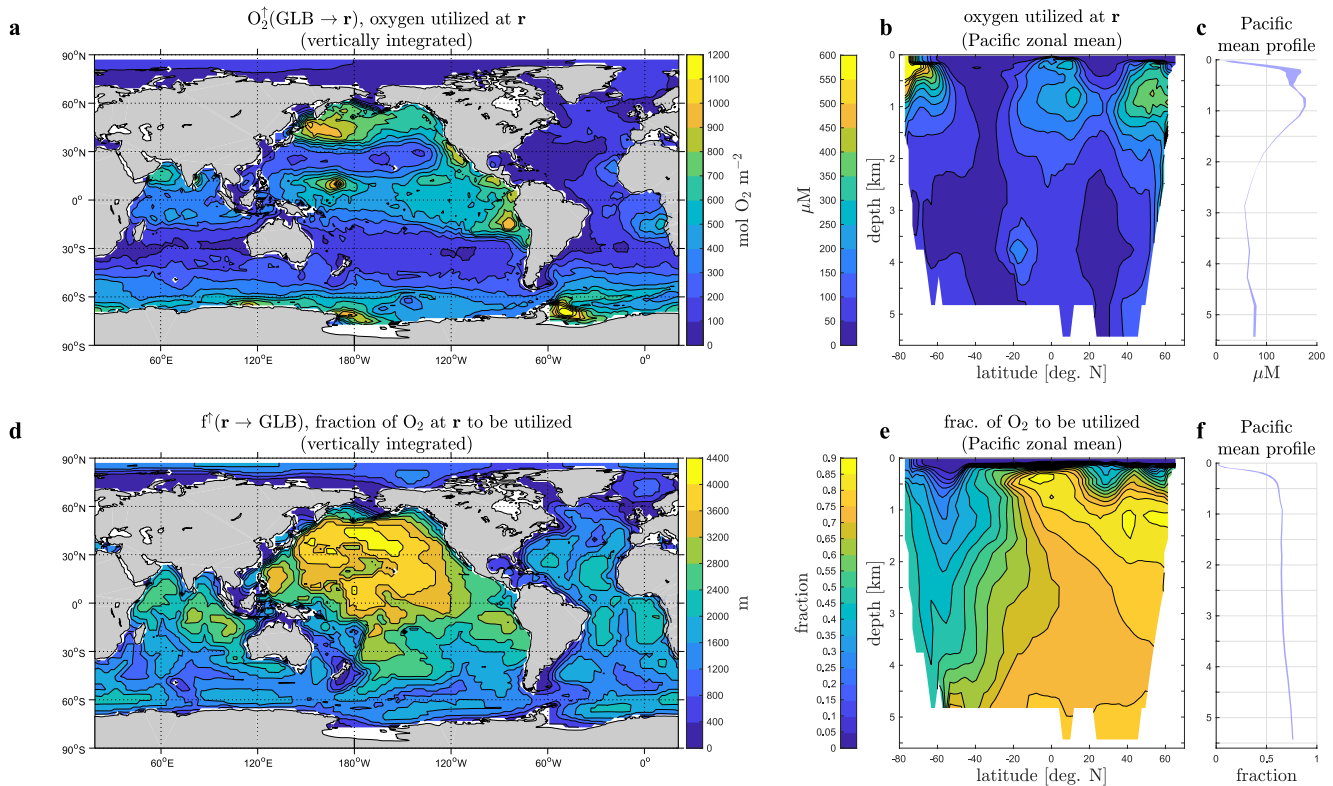


**Figure 6.**  $O_2^1(\text{GLB} \rightarrow \mathbf{r})$ , the amount of oxygen from anywhere in the global ocean that is lost to local respiration at  $\mathbf{r}$  per unit volume. Top plots: The vertical integral (a), Pacific zonal mean (b), and Pacific mean vertical profile (c) of  $O_2^1(\text{GLB} \rightarrow \mathbf{r})$ . Bottom plots: The vertical integral (d), Pacific zonal mean (e), and Pacific mean vertical profile (f) of  $f^l(\mathbf{r} \rightarrow \text{GLB})$ , the fraction of oxygen at  $\mathbf{r}$  that will be lost to respiration in the future while still in the ocean. The shading of the profiles shows their spread for a factor or  $\sim 3$  change in respiration timescale, with other parameters optimized.

birth to  $\mathbf{r}$  that spend a time  $\Gamma_{\text{ox},\Omega}^l$  in  $\Omega$ . In steady state this is the time for which the oxygen in  $\Omega$  sweeps past the respiration at point  $\mathbf{r}$  resulting in the downstream oxygen loss per unit volume given by 10.

Figures 6a–6c show  $O_2^1(\Omega \rightarrow \mathbf{r})$  for the case of  $\Omega$  being the global ocean (GLB). (Using the smaller interior regions  $\Omega$  (not shown) effectively selects the portion of  $O_2^1(\text{GLB} \rightarrow \mathbf{r})$  that lies within  $\Omega$  because the mean oxygen age accumulated within  $\Omega$  is largest for points within and downstream from  $\Omega$ .) Because  $O_2^1(\text{GLB} \rightarrow \mathbf{r})$  is the product of OUR and mean oxygen age,  $O_2^1(\text{GLB} \rightarrow \mathbf{r})$  is largest in the upper ocean (Figures 6b and 6c), with a horizontal distribution (Figure 6a) that is shaped by the structure of the mean oxygen age  $\Gamma_{\text{ox}}^l$ . The overall spatial structure of  $\Gamma_{\text{ox}}^l$  is similar to that of the ideal mean age  $\Gamma^l$ , with the oldest oxygen age being found in the middepth North Pacific and a tongue of old oxygen age reaching upward in the Southern Ocean due to upwelling circumpolar deep waters (Appendix D)  $O_2^1(\text{GLB} \rightarrow \mathbf{r})$  (Figure 6b) lie generally several hundred meters deeper in the water column than the maxima of  $\Delta O_2(\mathbf{r} \rightarrow \text{GLB})$  (Figures 5b and 5c) because the mean oxygen age goes to zero faster with decreasing depth than the mean water re-exposure time (Appendix D). This is in part because oxygen loss to respiration keeps the mean oxygen age relatively young in the upper ocean where respiration rates are high.

### 3.4.2. How Much of the Oxygen at a Given Point Will Be Utilized in $\Omega$ ?

Using a similar approach, we can calculate the fraction of the oxygen at every point that will be used for respiration within  $\Omega$  in the future. If the columns of matrix  $\chi$  are the time-evolving oxygen plumes due to the current oxygen in a given grid box (organized as  $\text{diag}([O_2])$ ), then  $\chi$  evolves according to

$$\partial_t \chi + \mathbf{A} \chi = \text{diag}([O_2]) \delta(t). \quad (11)$$

The  $\Omega$ -volume and time-integrated loss of each plume is thus given by  $w^T \Omega \int_0^\infty \mathbf{L} \chi dt = w^T \Omega \mathbf{L} \mathbf{A}^{-1} \text{diag}([O_2])$ . Each element of this row vector is the amount of oxygen that will be lost in  $\Omega$  due to oxygen that at  $t = 0$  is at the

**Table 1**  
Glossary of Key Quantities

symbol	Description	Units
$\Omega$	Specified region of the ocean (NP OMZ, PHZ, or entire ocean); also the mask for the region, with masking operator $\mathbf{\Omega} \equiv \text{diag}(\Omega)$	–
$\text{OUR}(\mathbf{r})$	Oxygen utilization rate at point $\mathbf{r}$	$\mu\text{M s}^{-1}$
$\Delta\text{O}_2(\mathbf{r})$	True oxygen utilization (TOU) at point $\mathbf{r}$ defined as $\Delta\text{O}_2 = [\text{O}_2]_{\text{pre}} - [\text{O}_2]$	$\mu\text{M}$
$\Delta\text{O}_2(\mathbf{r} \rightarrow \Omega)$	Contribution per unit volume to the $\Omega$ -integrated TOU at upstream point $\mathbf{r}$	$\mu\text{M}$
$\text{O}_2^{\uparrow}(\mathbf{r} \rightarrow \Omega)$	Oxygen concentration at $\mathbf{r}$ that will be utilized in $\Omega$	$\mu\text{M}$
$f^{\uparrow}(\mathbf{r} \rightarrow \Omega)$	Fraction of oxygen at $\mathbf{r}$ that will be utilized in $\Omega$	–
$\text{O}_2^{\uparrow}(\Omega \rightarrow \mathbf{r})$	Oxygen from $\Omega$ that will be lost at $\mathbf{r}$ per unit volume	$\mu\text{M}$
$\Gamma_{\Omega}^{\uparrow}(\mathbf{r})$	Mean water re-exposure time (time to next ventilation) at point $\mathbf{r}$ that accumulated in $\Omega$	years
$\Gamma_{\text{ox},\Omega}^{\uparrow}(\mathbf{r})$	Mean oxygen age (time since the oxygen entered from the atmosphere or was released by phytoplankton photosynthesis) accumulated in $\Omega$	years
$\delta q_{\text{TOU}}(\mathbf{r}_e)$	Response of $\Omega$ -integrated TOU to DIC uptake perturbation at euphotic-zone point $\mathbf{r}_e$ per unit volume of the perturbation	$\mu\text{M}$
$S_{\text{TOU}}$	Geographic sensitivity pattern of the $\Omega$ -integrated TOU (response per unit euphotic DIC uptake perturbation)	$(\text{mol O}_2) (\text{mol C})^{-1}$
$\mathbf{T}$	Advective-diffusive flux divergence operator	$\text{s}^{-1}$
$\mathbf{T}_a$	$\mathbf{T}$ plus fast relaxation to zero in ocean surface layer	$\text{s}^{-1}$
$\mathbf{K}$	Diagonal operator of air-sea exchange rate coefficients	$\text{s}^{-1}$
$\mathbf{L}$	Diagonal operator of oxygen utilization rate coefficients	$\text{s}^{-1}$
$\mathbf{A} = \mathbf{T} + \mathbf{K} + \mathbf{L}$	System operator for the linear-equivalent oxygen labels	$\text{s}^{-1}$

Note. DIC, dissolved inorganic carbon; NP OMZ, North Pacific oxygen minimum zone; PHZ, Pacific Hypoxic Zone; TOU, true oxygen utilization.

corresponding grid point. To obtain the concentration of this oxygen, denoted by  $\text{O}_2^{\uparrow}(\mathbf{r} \rightarrow \Omega)$ , we multiply from the right with  $\mathbf{W}^{-1}$ . For efficient computation, we take the transpose of the resulting expression to obtain the oxygen concentration at  $\mathbf{r}$  that will be utilized in  $\Omega$ :

$$\text{O}_2^{\uparrow}(\mathbf{r} \rightarrow \Omega) = \text{diag}([\text{O}_2]) \tilde{\mathbf{A}}^{-1} \mathbf{L} \Omega. \quad (12)$$

The fraction  $f^{\uparrow}(\mathbf{r} \rightarrow \Omega)$  of the oxygen at  $\mathbf{r}$  that will be lost to respiration in volume  $\Omega$  is thus given by

$$f^{\uparrow}(\mathbf{r} \rightarrow \Omega) = \tilde{\mathbf{A}}^{-1} \mathbf{L} \Omega. \quad (13)$$

Figures 6d–6f show the local fraction of oxygen  $f^{\uparrow}(\mathbf{r} \rightarrow \text{GLB})$  that will be utilized in respiration somewhere in the global ocean ( $\Omega = \text{GLB}$ ).  $f^{\uparrow}(\mathbf{r} \rightarrow \text{GLB})$  is largest in low-oxygen regions, where what little oxygen is available is likely to be utilized, and in the abyssal North Pacific. The high  $f^{\uparrow}(\mathbf{r} \rightarrow \text{GLB})$  fractions in the abyssal North Pacific are consistent with waters there taking around 1,400 years (Appendix D, see also Holzer, DeVries, & de Lavergne, 2021) to return to the surface giving ample opportunity for its oxygen content to be utilized. The vertical integral of the utilization fraction  $f^{\uparrow}(\mathbf{r} \rightarrow \text{GLB})$  (Figure 6d), measuring the height of the water column with an effective fraction of unity, exceeds 4,000 m in the central midlatitude North Pacific indicating that in this region most dissolved oxygen is destined for respiration within the ocean.

#### 4. Discussion

We developed new, quantitative relationships between the in situ OUR and the oxygen deficit of specified subsurface volumes  $\Omega$  by deriving the necessary transport timescales. (The glossary of Table 1 summarizes the key quantities involved.) These relationships hold for steady state, but they could be extended to time-dependent flow at the expense of additional complexity, which is beyond the scope of the present work. A key new insight from our analysis is that the timescale that connects the TOU of a given region with the upstream OUR is the mean time to *next* ventilation accumulated in the region,  $\Gamma_{\Omega}^{\uparrow}$ , and not the mean age of water in the region. A

complementary new result is that the mean oxygen age  $\Gamma_{\text{ox},\Omega}^{\downarrow}$  accumulated in the region (and not the mean water transit time) determines the amount of oxygen from  $\Omega$  that is respired downstream. The timescales  $\Gamma_{\Omega}^{\uparrow}$  and  $\Gamma_{\text{ox},\Omega}^{\downarrow}$  have, to the best of our knowledge, neither been defined nor calculated before. We emphasize that these timescales are distinct from the OMZ ventilation timescales calculated by Fu et al. (2018b). Ventilation timescales quantify the mean time since water in the OMZ was last at the surface, while  $\Gamma_{\Omega}^{\uparrow}$  and  $\Gamma_{\text{ox},\Omega}^{\downarrow}$  allow us to calculate, for the first time, how much of the oxygen lost at every point in the ocean contributes to the oxygen deficit in  $\Omega$  or results from the oxygen content of  $\Omega$ .

We acknowledge that the new relationships explored here cannot directly be applied to observational data because neither the mean re-exposure time nor the mean oxygen age can easily be inferred from readily available tracer observations. However, available tracer observations and hydrographic data can be assimilated into estimates of the ocean's advective-eddy-diffusive transport as has been done for the circulation model employed here. Once a data-assimilated transport model is available, the necessary timescales can easily be computed. Here we analyzed model-derived  $[\text{O}_2]$  and TOU using observed climatological  $[\text{O}_2]$  as a constraint on the biogeochemistry, but one could also combine model-derived timescales with directly observed oxygen fields.

A number of caveats apply to the simple data-constrained biogeochemical model used here to illustrate our analysis of oxygen in the ocean. Our model was inspired by the OCMIP approach (Najjar et al., 2007) and hence most parameters are globally uniform, although we did allow for flexible C:P stoichiometry (Teng et al., 2014; Galbraith & Martiny, 2015) (for details of implementation, see the work of Holzer, Kwon, and Pasquier (2021)). An important caveat for the oxygen component of the model is that the POC flux-divergence profile is parameterized by a Martin power law with a globally uniform exponent so that the model cannot capture the effects of temperature and oxygen-dependent POC respiration leading to increased particle preservation in OMZs (Keil et al., 2016; Cavan et al., 2017; Weber & Bianchi, 2020). While a significant fraction of respiration is thought to be due to benthic POC oxidization (e.g., Jahnke, 1996; Pan et al., 2014), in our OCIMP-style model there is no sediment burial and all POC, including all POC arriving in the bottom grid boxes, is dissolved with a 1-day e-folding timescale into semi-labile DOC. Modeled respiration acts only on this DOC pool with a globally uniform (optimized) timescale of  $\kappa_{\text{doc}}^{-1} \sim 3$  years that is also approximated as independent of the oxygen concentration as long as it remains above the suboxic minimum of  $\sim 5 \mu\text{M}$ . While the neglect of separating POC and DOC respiration may not be important for the oxygen distribution of a coarse-resolution model, the geographic uniformity of the POC flux-divergence profile (because of the neglect of its oxygen and temperature dependence), and hence of the DOC injection profile, likely contributes to model biases. Because the half-saturation constant of the oxygen dependence is estimated to be order  $10 \mu\text{M}$  (Laufkötter et al., 2017), the oxygen effect on POC flux for the larger PHZ ( $[\text{O}_2] \lesssim 65 \mu\text{M}$ ) should be reasonably small. However, the neglect of the temperature dependence of the POC flux (with  $q_{10}$  recently estimated as high as  $\sim 2.5$  (DeVries & Weber, 2017)) may well contribute to our model biases in the North Pacific, with a hypoxic region that is not vertically thick enough at high northern latitudes and too thick at low latitudes. The modeled OMZs likely also suffer from the coarse  $2^\circ \times 2^\circ$  resolution of the OCIM2 circulation: the equatorial current system which is important for the OMZ oxygen supply (Stramma et al., 2010) is poorly resolved by OCIM2. The model's single DOC pool (i.e., single respiration time scale) neglects regional variations in DOC lability (Pan et al., 2014) which may affect the distribution of OUR. (Available but sparse measurements of DOC and dissolved organic phosphate (Letscher & Moore, 2015) were not used as a direct constraint on the model.)

While a more detailed mechanistic model with temperature- and oxygen-dependent reaction rates and several DOC pools can be formulated (e.g., DeVries & Weber, 2017), such a model would necessarily introduce additional complexity and parameters, not all of which can be well constrained by the available observations. The complexity of the model used here is sufficient for illustrating our new oxygen diagnostics, and the shortcomings discussed should be mitigated through parameter optimization, with a threefold change in respiration timescale resulting in just a few percent changes in the oxygen metrics calculated here. We acknowledge, however, that a detailed analysis of the ocean's low-oxygen regions would benefit from a more detailed biogeochemical model to reduce the remaining biases, and the modeling of OMZs would additionally benefit from higher spatial resolution.



## 5. Conclusions

We have investigated the sensitivities of the oxygen content of key interior ocean regions,  $\Omega$ , to point-wise changes in euphotic organic-matter production, with emphasis on the large low-oxygen regions of the Pacific. To better understand the controls on these sensitivities and the fate of oxygen in the ocean, we developed new diagnostics to reveal where the respiration occurs that leads to the oxygen deficit in  $\Omega$ , and how much of the oxygen at any point will be utilized in the future. Our analysis establishes previously unexplored steady-state timescales that link the in situ OUR with the TOU on one hand, and with the oxygen to be lost in the future on the other hand. The TOU sensitivities and our new oxygen diagnostics were illustrated using a simple data-constrained, steady-state model of the phosphorus, carbon, and oxygen cycles that is embedded in a data-assimilated global circulation (OCIM2) representative of the current climatology. Our key findings are as follows:

Globally integrated, the ocean's oxygen content is most sensitive to biological productivity changes in the major deep-water formation regions, where increased organic-matter respiration strips oxygen out of cold, well-oxygenated deep waters. For the PHZ and the NP OMZ, the integrated TOU is most sensitive in the mid-latitude North and South Pacific where mode and intermediate waters form that directly ventilate these regions as well as in the eastern tropical Pacific where stimulated particulate organic-matter export increases the respiration rate directly within the low-oxygen regions. Because biogenic particles and freshly ventilated oxygen access different density classes, the sensitivity pattern is broader and more complex than the pattern of ventilation.

The sensitivity pattern of the  $\Omega$ -integrated TOU is controlled by where the utilization occurs that contributes to the oxygen deficit in  $\Omega$ . In steady state, these contributions per unit volume at point  $\mathbf{r}$  are given by  $\Delta O_2(\mathbf{r} \rightarrow \Omega) = \text{OUR}(\mathbf{r}) \Gamma_{\Omega}^{\downarrow}(\mathbf{r})$ , where  $\Gamma_{\Omega}^{\downarrow}(\mathbf{r})$  is the mean time that water at  $\mathbf{r}$  spends in  $\Omega$  on its way to *next* ventilation at the surface. Exploiting the relatively short lifetime of semilabile DOC, TOU sensitivity patterns can be approximated by the [DOC]-weighted (or OUR-weighted) vertical integral of  $\Gamma_{\Omega}^{\downarrow}(\mathbf{r})$ . This quantifies that sensitivity is highest where the water containing the organic-matter plume beneath the perturbed production has the best  $\Omega$  access in terms of the amount of time spent in  $\Omega$  as it wends its way back to its next surface re-exposure. The loss of oxygen  $\Delta O_2(\mathbf{r} \rightarrow \Omega)$  that causes the oxygen deficit of the Pacific low-oxygen regions is largest in the upper ocean with maxima at  $\sim 250$  m depth in our model.

The amount of oxygen from interior region  $\Omega$  that is utilized per unit volume at point  $\mathbf{r}$  is in steady state given by  $O_2^{\downarrow}(\Omega \rightarrow \mathbf{r}) = \text{OUR}(\mathbf{r}) \Gamma_{\text{ox},\Omega}^{\downarrow}(\mathbf{r})$ , where  $\Gamma_{\text{ox},\Omega}^{\downarrow}(\mathbf{r})$  is the mean age of oxygen at  $\mathbf{r}$  (since “birth” by injection from the atmosphere and phytoplankton photosynthesis) that was accumulated in  $\Omega$  on the way to  $\mathbf{r}$ . Oxygen “dies” either by escape to the atmosphere or by utilization and the mean oxygen age is hence everywhere younger than the ideal mean water age. The mean oxygen age also attenuates to zero faster with decreasing depth than the mean re-exposure time so that  $O_2^{\downarrow}(\Omega \rightarrow \mathbf{r})$ , the loss of oxygen from  $\Omega$ , generally occurs deeper in the water column (lower thermocline) than the loss  $\Delta O_2(\mathbf{r} \rightarrow \Omega)$  leading to the oxygen deficit of  $\Omega$ .

The fraction of the oxygen at a given point in the ocean that will be utilized somewhere in the ocean is highest in the North Pacific, where its zonal mean exceeds 90% in the PHZ and 70% throughout the water column beneath with a local benthic maximum. This quantifies that where there is little oxygen, a larger fraction is likely to be utilized and is consistent with the fact that North Pacific abyssal waters take on average around 1,400 years to be ventilated again (e.g., DeVries & Primeau, 2011; Holzer, DeVries, & de Lavergne, 2021), providing ample time for utilization.

In the coming decades and centuries not only the ocean's ecosystems will change but also its circulation and physical state. The analysis of sensitivity to changes in production and our new diagnostics for determining the fate of oxygen in ocean biogeochemical models will be useful for disentangling the effects of changing biology and changing circulation in the future ocean.

## Appendix A: Objective Function and Optimized Parameter Values

The objective function,  $E$ , is constructed from the mismatches  $\delta\chi = \chi_{\text{mod}} - \chi_{\text{obs}}$  for a given tracer concentration  $\chi$ . Organizing these fields into column vectors, normalizing the volume-weighted squared mismatch of a given tracer by its global spatial variance, and weighting the thus normalized quadratic mismatches for each tracer field ( $O_2$ , DIC,  $PO_4$ , TA) equally, the objective function  $E$  is given by

**Table A1**  
Numerical Values of Key Biogeochemical Parameters (\* Not Optimized) and Fit Metrics

Parameter	Description	Value		Units
		( $\kappa_{\text{doc}}$ optimized)	( $\kappa_{\text{doc}}$ prescribed)	
$\kappa_{\text{doc}}^{-1} = \kappa_{\text{dop}}^{-1}$	Respiration timescale	$3.2 \pm 0.2$	1.2*	Years
$\sigma$	Fraction of DOM production	$0.2817 \pm 0.0007$	$0.552 \pm 0.005$	–
$\alpha$	Production amplitude	$59. \pm 6.$	$98. \pm 1.$	$\mu\text{M C/year}$
$\beta$	Production NPP exponent	$0.05 \pm 0.05$	$0.04 \pm 0.01$	–
$b$	Martin exponent	$1.009 \pm 0.007$		–
$R_{\text{O}_2:\text{C}}$	O <sub>2</sub> :C stoichiometry	$1.307 \pm 0.002$		$\text{mol O}_2/(\text{mol C})$
$R$	PIC/POC rain ratio	$6.2 \pm 0.1$		%
$L_{\text{PIC}}$	PIC remin. length	4.50*		km
$k_{\text{poc}}^{-1} = k_{\text{pop}}^{-1} = k_{\text{pic}}^{-1}$	Particle dissolution timescales		1*	Days
$m_{\text{PC}}$	$d(\text{P:C})/d[\text{PO}_4]$		3.30	$(\mu\text{M PO}_4)^{-1}$
$b_{\text{PC}}$	P:C intercept at $[\text{PO}_4] = 0$		7.12	–
–	RMS mismatch of O <sub>2</sub>		$20.36 \pm 0.07$	$\mu\text{M}$
–	RMS mismatch of DIC		$19.8 \pm 0.1$	$\mu\text{M}$
–	RMS mismatch of PO <sub>4</sub>		$0.155 \pm 0.002$	$\mu\text{M}$
–	RMS mismatch of TA		$13.82 \pm 0.07$	$\mu\text{M}$
–	(Total mismatch variance, $E/4$ )		$7.35 \pm 0.05$	%

Note. DIC, dissolved inorganic carbon; NPP, net primary productivity; POC, particulate organic carbon; RMS, root-mean-square; TA, total alkalinity.

$$E = \frac{\delta\text{O}_2^T \hat{\mathbf{w}} \delta\text{O}_2}{\sigma_{\text{O}_2}^2} + \frac{\delta\text{DIC}^T \hat{\mathbf{w}} \delta\text{DIC}}{\sigma_{\text{DIC}}^2} + \frac{\delta\text{PO}_4^T \hat{\mathbf{w}} \delta\text{PO}_4}{\sigma_{\text{PO}_4}^2} + \frac{\delta\text{TA}^T \hat{\mathbf{w}} \delta\text{TA}}{\sigma_{\text{TA}}^2}, \quad (\text{A1})$$

where  $\sigma_\chi^2 = (\chi - \bar{\chi})^T \hat{\mathbf{w}} (\chi - \bar{\chi})$  is the spatial variance  $\chi$  (overbar denotes the volume-weighted global mean), and  $\hat{\mathbf{w}} = \text{diag}(\hat{w})$ , where  $\hat{w}$  is the vector of grid-box-volume weights.  $E$  is minimized numerically to determine the optimized parameters values collected in Table A1, which also shows the corresponding root-mean-square (RMS) values for the mismatch between model and observations. For the definitions of the carbon-cycle parameters  $\alpha$ ,  $\beta$ ,  $m_{\text{PC}}$ ,  $b_{\text{PC}}$ ,  $L_{\text{PIC}}$ ,  $R$  and  $k_{\text{pop}}$ ,  $k_{\text{pic}}$  see the work of Holzer, Kwon, and Pasquier (2021). The joint volume-weighted distribution of the model concentrations and corresponding observations (in essence a binned scatter plot of modeled vs. observed values) is shown for all four tracers in Figure A1 for the case of VGPM-based uptake and optimized respiration timescale.

For an ad-hoc assessment of uncertainty, we performed our calculations with four different versions of the biogeochemical model: Optimized and specified DOC respiration timescale  $\kappa_{\text{doc}}^{-1}$ , and biological production based on VGPM-based and GbPM-based NPP. We did not optimize all parameters but adopted the remineralization length scale for calcium carbonate and the parameters of the C:P stoichiometry from the parent carbon model. The differences among optimized biogeochemical models are dominated by the value of  $\kappa_{\text{doc}}$ . However, because the other parameters that shape biological production ( $\sigma$ ,  $\alpha$ , and  $\beta$ ) are also optimized, the resulting oxygen fields vary little (less than 6% below 250 m for  $[\text{O}_2]$  in the zonal mean) for a roughly threefold change in  $\kappa_{\text{doc}}$ . In Table A1, we list the values of  $\kappa_{\text{doc}}$ ,  $\sigma$ ,  $\alpha$ , and  $\beta$  separately for the optimized and specified  $\kappa_{\text{doc}}$  cases; the small uncertainties in the numerical values quantify the small sensitivity to the choice of NPP product. For parameter and RMS mismatch values that do not strongly depend of the value of  $\kappa_{\text{doc}}$ , Table A1 lists the mean and half-range across all four model versions.

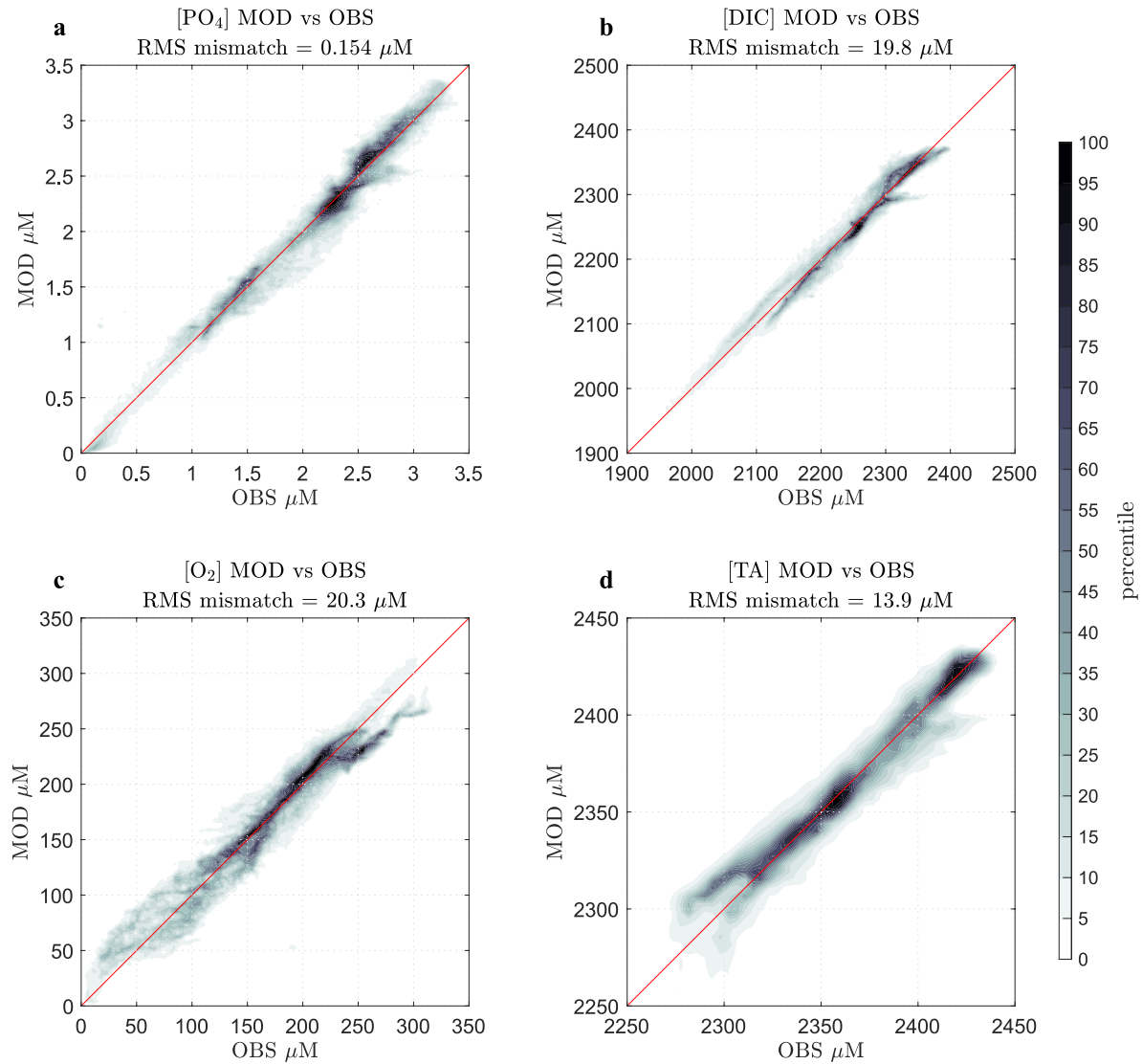


**Figure A1.** Joint volume-weighted distribution of the observed and modeled concentrations of  $\text{PO}_4$  (a), dissolved inorganic carbon (DIC) (b),  $[\text{O}_2]$  (c), and  $[\text{TA}]$  (equivalent to the binned scatter plot of modeled vs. observed values.) The percentiles of the cumulative distribution are defined such that  $x\%$  of the distribution lies outside the  $x$ -percentile contour. Large percentiles thus correspond to high densities. The corresponding volume-weighted root-mean-square (RMS) mismatch is provided in the plot titles.

## Appendix B: Sensitivity Analysis

### B1. Linearization and Sensitivity of the Oxygen-Carbon System

To calculate the sensitivity to point-wise small-amplitude perturbations  $\delta U_C$  in biological production, we linearize the OUR term of Equation 1. The linearized and discretized Equation 1 for the responses  $\delta[\text{O}_2]$ ,  $\delta[\text{DOC}]$ , and  $\delta[\text{POC}]$  can be written as

$$\frac{d}{dt} \begin{bmatrix} \delta[\text{O}_2] \\ \delta[\text{DOC}] \\ \delta[\text{POC}] \end{bmatrix} + \begin{bmatrix} \mathbf{T} + \mathbf{K} + \text{diag} \left( \frac{\partial \text{OUR}}{\partial [\text{O}_2]} \right) & \text{diag} \left( \frac{\partial \text{OUR}}{\partial [\text{DOC}]} \right) & 0 \\ 0 & \mathbf{T} + \kappa_{\text{doc}} \mathbf{I} & -k_{\text{poc}} \mathbf{I} \\ 0 & 0 & \mathbf{T} + k_{\text{poc}} \mathbf{I} \end{bmatrix} \begin{bmatrix} \delta[\text{O}_2] \\ \delta[\text{DOC}] \\ \delta[\text{POC}] \end{bmatrix} = \begin{bmatrix} R_{\text{O}_2:\text{C}} \delta U_C \\ \sigma \delta U_C \\ (1 - \sigma) \delta U_C \end{bmatrix} \quad (\text{B1})$$

where  $\mathbf{I}$  is the  $N \times N$  identity matrix and the partial derivatives are evaluated at the unperturbed based state. We now replace the perturbation field (a single column vector)  $\delta U_C$  by a matrix each column of which contains only a single grid box of perturbed uptake, with zeros elsewhere. That is, we change the right-hand-side of Equation B1 to  $\delta \mathbf{Y} = [R_{O_2:C}, \sigma, (1 - \sigma)]^T \otimes \mathbf{diag}(\delta U_C)$ , so that every column of the solution  $\delta \mathbf{X}$  of the linearized system  $\mathbf{M} \delta \mathbf{X} = \delta \mathbf{Y}$  is the response field from perturbing biological production at a single grid point.

Finding  $\delta \mathbf{X}$  would require as many solutions as there are euphotic grid points (we do not consider perturbations in the aphotic zone where  $U_C$  is zero), which is numerically very inefficient. We therefore focus on the steady-state responses  $\delta \mathbf{X}$ , or more generally on a linear transformation  $\mathbf{F} \delta \mathbf{X}$  of these responses, volume integrated over  $\Omega$  which can be computed efficiently by taking the adjoint. (The operator  $\mathbf{F}$  required for computing the TOU response is derived in the next subsection.) With vector  $w$  of grid-box volumes, and defining  $\mathbf{W} \equiv \mathbf{diag}(W)$  and  $\mathbf{\Omega} \equiv \mathbf{diag}(\Omega)$ , we are interested in the  $\Omega$ -integrated response  $\delta Q^T \equiv w^T \mathbf{\Omega} \mathbf{F} \delta \mathbf{X}$ . It is natural to work with the response per unit volume of the perturbed grid box  $\delta q^T \equiv \delta Q^T w^{-1}$ , which on taking the transpose, and using  $\delta \mathbf{X} = \mathbf{M}^{-1} \delta \mathbf{Y}$ , can be written as

$$\delta q = \delta \tilde{\mathbf{Y}} \tilde{\mathbf{M}}^{-1} \tilde{\mathbf{F}} \mathbf{\Omega}, \quad (\text{B2})$$

where the adjoint of an operator  $\mathbf{O}$  with respect to the volume-weighted inner product is given by  $\tilde{\mathbf{O}} \equiv \mathbf{W}^{-1} \mathbf{O}^T \mathbf{W}$ . Thus,  $\delta q$  is the  $\Omega$ -integrated response, per perturbation-grid-box volume, mapped to the grid boxes where the perturbation occurred, which can be computed through a single matrix inversion of  $\tilde{\mathbf{M}}$  (in practice computed by solving the corresponding linear system).

## B2. Response of TOU in Terms of Response in Oxygen and Carbon

TOU is defined as  $\Delta O_2 = [O_2]_{\text{pre}} - [O_2]$  so that the response of TOU to perturbations is  $\delta \Delta O_2 = \delta [O_2]_{\text{pre}} - \delta [O_2]$ . In the limit of small-amplitude perturbations,  $\delta O_2$  is available from the solution  $\delta X = [\delta [O_2], \delta [\text{DOC}], \delta [\text{POC}]]^T$  of the linearization (B1).  $[O_2]_{\text{pre}}$  is the response to the specified boundary condition that  $[O_2]_{\text{pre}} = [O_2]$  in the euphotic zone, which we enforce through fast relaxation with  $\mathbf{L}_a \equiv \mathbf{diag}(\Omega_{\text{eu}}/\tau)$  so that  $\mathbf{T} [O_2]_{\text{pre}} = \mathbf{L}_a ([O_2] - [O_2]_{\text{pre}})$  giving  $[O_2]_{\text{pre}} = \mathbf{T}_a^{-1} \mathbf{L}_a [O_2]$ , where  $\mathbf{T}_a \equiv \mathbf{T} + \mathbf{L}_a$ . Thus,  $\delta [O_2]_{\text{pre}} = \mathbf{T}_a^{-1} \mathbf{L}_a \delta [O_2]$  and  $\delta \Delta [O_2] = (\mathbf{T}_a^{-1} \mathbf{L}_a - \mathbf{I}) \delta [O_2]$  so that the operator  $\mathbf{F}$  needed to compute the TOU response is given by

$$\mathbf{F} = \mathbf{diag}([1, 0, 0]) \otimes (\mathbf{T}_a^{-1} \mathbf{L}_a - \mathbf{I}), \quad (\text{B3})$$

where the  $\mathbf{diag}([1, 0, 0])$  simply selects the  $\delta [O_2]$  part of the system response  $\delta X$ .

## Appendix C: Link Between TOU Sensitivity Pattern and Mean Re-exposure Time

From Equations 6 and 7 of the main text, it follows that the response of the  $\Omega$ -integrated TOU to a perturbation  $d^2 r' \delta U_C dz'$  (integrated over a water column of cross-sectional area  $d^2 r'$ ) is given by

$$\delta Q_{\text{TOU}} \equiv \int_{\Omega} \delta (\Delta O_2) d^3 r = \int_{\text{ocean}} \Gamma_{\Omega}^{\dagger}(\mathbf{r}) \delta \text{OUR}(\mathbf{r}) d^3 r. \quad (\text{C1})$$

We can now exploit the short lifetime ( $\sim 3$  years for our optimized state) of DOC to approximate the response  $\delta \text{OUR}$  as horizontally collocated with the production perturbation  $\delta U_C$  and with zero  $\delta \text{OUR}$  outside the perturbed water column. Thus, the global integral on the right-hand-side of Equation C1 can be approximated by the vertical integral at the point of perturbation:  $\delta Q_{\text{TOU}} \sim d^2 r' \int \Gamma_{\Omega}^{\dagger}(\mathbf{r}') \delta \text{OUR}(\mathbf{r}') dz'$ , where  $\mathbf{r}'$  are the coordinates of the perturbed water column. To a good approximation  $\delta \text{OUR} \simeq R_{O_2:C} \kappa_{\text{doc}} \delta [\text{DOC}]$ , and furthermore  $\delta [\text{DOC}] \sim \mu [\text{DOC}]$ , that is, the DOC perturbation is proportional to DOC (proportionality coefficient  $\mu$ ) because the amplitude of the DOC plume beneath a given euphotic location is proportional to its biological production, and the plume profile is shaped, at least in our model, by the Martin curve for POC flux divergence regardless of production amplitude. Thus, we also have that  $\int \delta U_C dz' \sim \kappa_{\text{doc}} \int \delta [\text{DOC}] dz \sim \mu \kappa_{\text{doc}} \int [\text{DOC}] dz$ . Expressing  $\delta Q_{\text{TOU}}$  in terms of the response  $\delta q_{\text{TOU}}$  per unit volume,  $\delta Q_{\text{TOU}} = d^2 r' \int \delta q dz'$ , we obtain the approximate expression for the sensitivity of the  $\Omega$ -integrated TOU

$$S_{\text{TOU}} = \frac{\int \delta q_{\text{TOU}} dz}{\int \delta U_C dz} \simeq R_{\text{O}_2\text{C}} \frac{\int \Gamma_{\Omega}^{\dagger} [\text{DOC}] dz}{\int [\text{DOC}] dz} \simeq R_{\text{O}_2\text{C}} \frac{\int \Gamma_{\Omega}^{\dagger} \text{OUR} dz}{\int \text{OUR} dz}, \quad (\text{C2})$$

that is, the sensitivity map of the  $\Omega$ -integrated TOU is approximately proportional to the OUR-weighted (in our model approximately equivalent to the DOC-weighted) vertical average of  $\Gamma_{\Omega}^{\dagger}$ , the mean re-exposure time accumulated in region  $\Omega$ .

## Appendix D: Mean Ages and Re-exposure Times for Water and Oxygen

The main text considered the mean water re-exposure time  $\Gamma^{\dagger}$ , the mean oxygen age  $\Gamma_{\text{ox}}^{\dagger}$ , and their  $\Omega$ -accumulated counterparts. Here we develop these quantities and, for completeness, also the ideal mean water age  $\Gamma^{\downarrow}$  and the oxygen re-exposure time  $\Gamma_{\text{ox}}^{\downarrow}$ .

In its simplest form, the ideal mean age (of water)  $\Gamma^{\downarrow}$  can be considered to obey  $D\Gamma/Dt = 1$  subject to the boundary condition  $\Gamma^{\downarrow} = 0$  at the surface, where  $D/Dt$  is the total time derivative including the advective and diffusive flux divergences. Thus following a fluid element with the advective-diffusive flow,  $\Gamma^{\downarrow}$  is an age that simply increases at the chronological unit rate everywhere and is reset to zero at the surface. We can define the mean age  $\Gamma_{\Omega}^{\downarrow}$  accumulated in a subregion  $\Omega$ , by allowing the mean age to only increase in  $\Omega$ . In steady state we have

$$\mathbf{T} \Gamma_{\Omega}^{\downarrow} = \Omega + \mathbf{L}_a (0 - \Gamma_{\Omega}^{\downarrow}), \quad (\text{D1})$$

where the last term enforces the boundary condition of  $\Gamma_{\Omega}^{\downarrow} = 0$  in the euphotic zone via fast relaxation. In terms of  $\mathbf{T}_a = \mathbf{T} + \mathbf{L}_a$  we thus obtain  $\Gamma_{\Omega}^{\downarrow} = \mathbf{T}_a^{-1} \Omega$ . Note that summing over all interior regions covering the entire ocean volume (without overlap or gaps) produces the usual ideal mean age:  $\sum_{\Omega} \Gamma_{\Omega}^{\downarrow} = \Gamma^{\downarrow}$ . Figure D1a shows the Pacific zonal mean of the ideal mean age, and Figure D1e shows the ideal mean age accumulated in the PHZ.

The mean re-exposure time (of water) can be thought of as the mean age for the time-reversed adjoint flow (Holzer & Hall, 2000), and thus in steady state,  $\Gamma_{\Omega}^{\dagger}$ , the mean re-exposure time accumulated in  $\Omega$  obeys

$$\tilde{\mathbf{T}} \Gamma_{\Omega}^{\dagger} = \Omega + \mathbf{L}_a (0 - \Gamma_{\Omega}^{\dagger}), \quad (\text{D2})$$

so that  $\Gamma_{\Omega}^{\dagger} = \tilde{\mathbf{T}}_a^{-1} \Omega$  and again  $\sum_{\Omega} \Gamma_{\Omega}^{\dagger} = \Gamma^{\dagger}$ . Figure D1b shows the Pacific zonal mean of the mean re-exposure time,  $\Gamma^{\dagger}$ , and Figure D1f shows the mean re-exposure time accumulated in the PHZ ( $\Gamma_{\Omega}^{\dagger}$  with  $\Omega = \text{PHZ}$ ).

To define mean oxygen age and mean oxygen re-exposure times, we consider oxygen to be “born” by the source  $S \equiv S_{\text{atm}} + S_{\text{bio}}$  (one could also separately consider atmospheric and photosynthetic oxygen) and oxygen to “die” through utilization or escape to the atmosphere. The (not yet normalized) distribution  $\mathcal{G}_{\text{ox}}$  of times since birth thus obeys for steady-state flow

$$\partial_t \mathcal{G}_{\text{ox}} + \mathbf{A} \mathcal{G}_{\text{ox}} = S \delta(t) \quad (\text{D3})$$

where  $\mathbf{A} = \mathbf{T} + \mathbf{K} + \mathbf{L}$  includes the transport and death processes. The mean oxygen age is then given by  $\Gamma_{\text{ox}}^{\downarrow} = \langle t \mathcal{G}_{\text{ox}} \rangle / \langle \mathcal{G}_{\text{ox}} \rangle$  (element-wise ratio), where  $\langle \dots \rangle \equiv \int_0^{\infty} \dots dt$ , or equivalently by  $\Gamma_{\text{ox}}^{\downarrow} = \langle t \hat{\mathcal{G}}_{\text{ox}} \rangle$ , where  $\hat{\mathcal{G}}_{\text{ox}} \equiv \mathbf{diag}^{-1}([\text{O}_2]) \mathcal{G}_{\text{ox}}$  is the normalized distribution of times since birth as it follows from Equation D3 that  $\langle \mathcal{G}_{\text{ox}} \rangle = \mathbf{A}^{-1} S = [\text{O}_2]$ . From Equation D3 it is straightforward to show that  $\hat{\mathbf{A}} \Gamma_{\text{ox}}^{\downarrow} = 1$ , where  $\hat{\mathbf{A}} = \mathbf{diag}^{-1}([\text{O}_2]) \mathbf{A} \mathbf{diag}([\text{O}_2])$ , that is, the mean oxygen age increases everywhere at the chronological unit rate (and decreases through utilization and escape to the atmosphere which are built into  $\mathbf{A}$ ). We obtain the mean oxygen age accumulated in  $\Omega$  by letting the mean oxygen age only advance in  $\Omega$ , that is,

$$\hat{\mathbf{A}} \Gamma_{\text{ox},\Omega}^{\downarrow} = \Omega, \quad (\text{D4})$$

so that  $\Gamma_{\text{ox},\Omega}^{\downarrow} = \hat{\mathbf{A}}^{-1} \Omega = \mathbf{diag}^{-1}([\text{O}_2]) \mathbf{A}^{-1} \Omega [\text{O}_2]$  and again  $\sum_{\Omega} \Gamma_{\text{ox},\Omega}^{\downarrow} = \Gamma_{\text{ox}}^{\downarrow}$ . Figure D1c shows the Pacific zonal mean of the full oxygen age, and Figure D1g shows the oxygen age accumulated in the PHZ. Note that the mean

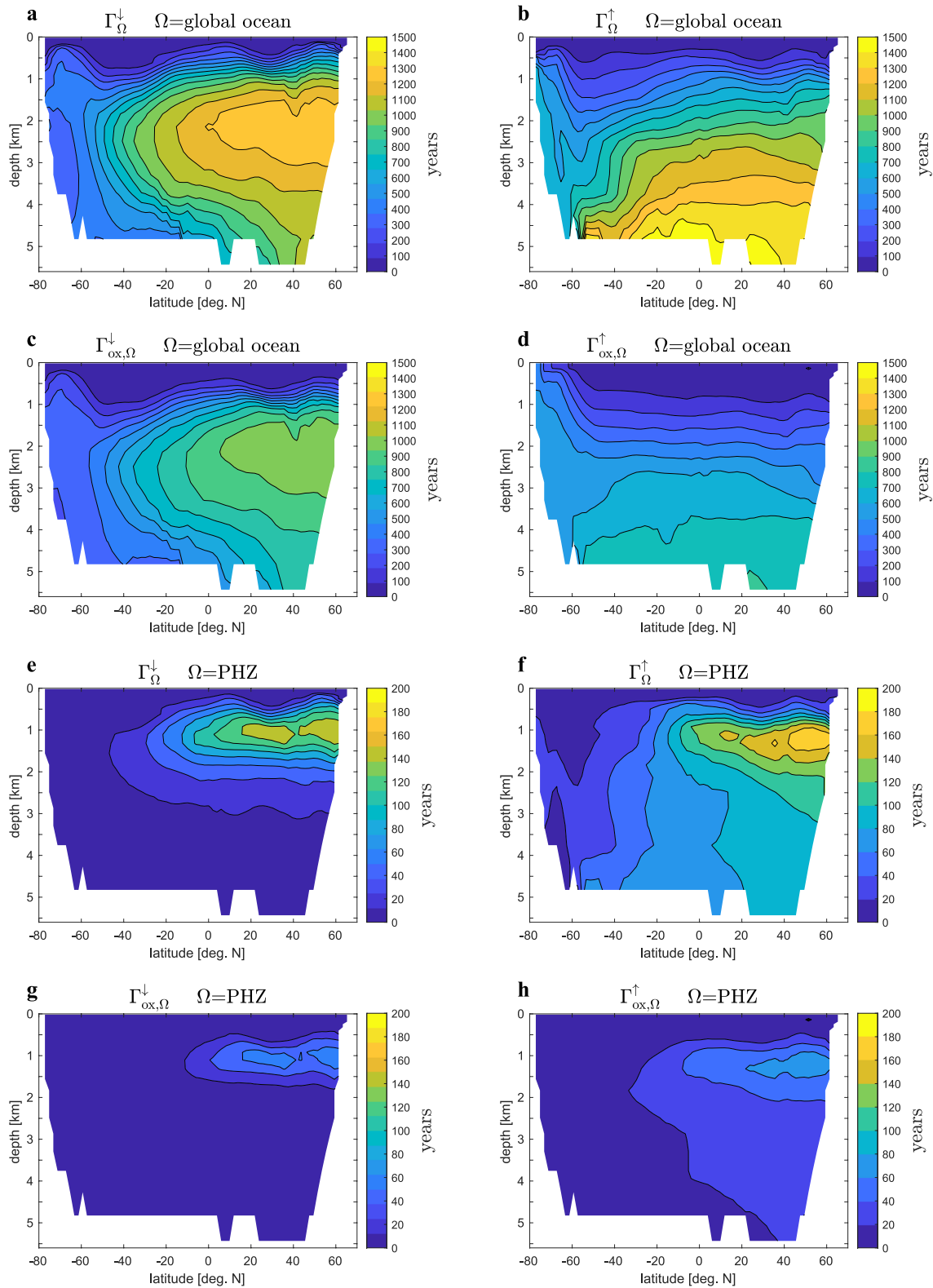


**Figure D1.** Pacific zonal means of key mean transit times: The ideal mean age  $\Gamma^{\downarrow}$  (a), the mean re-exposure time  $\Gamma^{\uparrow}$  (b), the mean oxygen age  $\Gamma_{ox}^{\downarrow}$  (c), and the oxygen mean re-exposure time  $\Gamma_{ox}^{\uparrow}$  (d). Plots (e–h) show the corresponding mean times accumulated in the Pacific Hypoxic Zone (PHZ). (Note the different color scale for the  $\Omega$ -accumulated timescales).

oxygen ages have lower overall amplitude and are much younger near the surface than their water counterparts because the surface-intensified oxygen utilization provides an additional death process that does not act on water itself.

An oxygen mean “re-exposure” time, with “re-exposure” meaning either return to the atmosphere or utilization in respiration, can be analogously developed. One obtains  $\Gamma_{\text{ox},\Omega}^{\uparrow} = \mathbf{diag}^{-1}([\text{O}_2]) \tilde{\mathbf{A}}^{-1} [\text{O}_2]$ , the Pacific zonal mean of which is shown in Figure D1d and D1h.

## Data Availability Statement

The oxygen data used are available at <https://www.nodc.noaa.gov/ocads/oceans/GLODAPv2>. (Availability of the data used for the associated parent carbon model has been detailed in the work of Holzer, Kwon, and Pasquier (2021).) Optimizations were carried out on the Katana computational cluster supported by Research Technology Services at UNSW Sydney (<https://dx.oii.org/10.26190/669x-a286>).

## Acknowledgments

This work was supported by Australian Research Council grant DP210101650.

## References

- Behrenfeld, M. J., & Falkowski, P. G. (1997). Photosynthetic rates derived from satellite-based chlorophyll concentration. *Limnology & Oceanography*, 42, 1–20. <https://doi.org/10.4319/lo.1997.42.1.0001>
- Broecker, W. S., & Peng, T. H. (1982). *Tracers in the sea* (p. 690). Eldigio Press, Lamont Doherty Geological Observatory.
- Cabr e, A., Marinov, I., Bernardello, R., & Bianchi, D. (2015). Oxygen minimum zones in the tropical Pacific across CMIP5 models: Mean state differences and climate change trends. *Biogeosciences*, 12(18), 5429–5454. <https://doi.org/10.5194/bg-12-5429-2015>
- Cavan, E., Trimmer, M., Shelley, F., & Sanders, R. (2017). Remineralization of particulate organic carbon in an ocean oxygen minimum zone. *Nature Communications*, 8(1), 14847. <https://doi.org/10.1038/ncomms14847>
- DeVries, T. (2014). The oceanic anthropogenic CO<sub>2</sub> sink: Storage, air-sea fluxes, and transports over the industrial era. *Global Biogeochemical Cycles*, 28(7), 631–647. <https://doi.org/10.1002/2013gb004739>
- DeVries, T., & Holzer, M. (2019). Radiocarbon and helium isotope constraints on deep-ocean ventilation and mantle-<sup>3</sup>He sources. *Journal of Geophysical Research: Oceans*, 124(5), 3036–3057. <https://doi.org/10.1002/2018JC014716>
- DeVries, T., & Primeau, F. (2011). Dynamically and observationally constrained estimates of water-mass distributions and ages in the global ocean. *Journal of Physical Oceanography*, 41(12), 2381–2401. <https://doi.org/10.1175/JPO-D-10-05011.1>
- DeVries, T., & Weber, T. (2017). The export and fate of organic matter in the ocean: New constraints from combining satellite and oceanographic tracer observations. *Global Biogeochemical Cycles*, 31(3), 535–555. <https://doi.org/10.1002/2016GB005551>
- Emerson, S. R., & Hedges, J. I. (2008). *Chemical oceanography and the marine carbon cycle* (p. 453). Cambridge University Press.
- Fu, W., Bardin, A., & Primeau, F. (2018). Tracing ventilation source of tropical Pacific oxygen minimum zones with an adjoint global ocean transport model. *Deep-Sea Research Part I*, 139, 95–103. <https://doi.org/10.1016/j.dsr.2018.07.017>
- Fu, W., Primeau, F., Moore, J. K., Lindsay, K., & Randerson, J. T. (2018). Reversal of increasing tropical ocean hypoxia trends with sustained climate warming. *Global Biogeochemical Cycles*, 32(4), 551–564. <https://doi.org/10.1002/2017GB005788>
- Galbraith, E. D., & Martiny, A. C. (2015). A simple nutrient-dependence mechanism for predicting the stoichiometry of marine ecosystems. *Proceedings of the National Academy of Sciences*, 112(27), 8199–8204. <https://doi.org/10.1073/pnas.1423917112>
- Garcia, H. E., Locarnini, R. A., Boyer, T. P., & Antonov, J. I. (2010). *World Ocean Atlas 2009, volume 4: Nutrients (phosphate, nitrate, silicate)*. In S. Levitus (Ed.), (p. 398). U.S. Government Printing Office.
- Helm, K. P., Bindoff, N. L., & Church, J. A. (2011). Observed decreases in oxygen content of the global ocean. *Geophysical Research Letters*, 38(23), L23602. <https://doi.org/10.1029/2011GL049513>
- Holzer, M., DeVries, T., & de Lavergne, C. (2021). Diffusion controls the ventilation of a Pacific shadow zone above abyssal overturning. *Nature Communications*, 12(1), 4348. <https://doi.org/10.1038/s41467-021-24648-x>
- Holzer, M., & Hall, T. M. (2000). Transit-time and tracer-age distributions in geophysical flows. *Journal of the Atmospheric Sciences*, 57(21), 3539–3558. [https://doi.org/10.1175/1520-0469\(2000\)057<3539:ttatad>2.0.co;2](https://doi.org/10.1175/1520-0469(2000)057<3539:ttatad>2.0.co;2)
- Holzer, M., Kwon, E. Y., & Pasquier, B. (2021). A new metric of the biological carbon pump: Number of pump passages and its control on atmospheric pCO<sub>2</sub>. *Global Biogeochemical Cycles*, 35(6), e2020GB006863. <https://doi.org/10.1029/2020GB006863>
- Holzer, M., Primeau, F. W., DeVries, T., & Matear, R. (2014). The Southern Ocean silicon trap: Data-constrained estimates of regenerated silicic acid, trapping efficiencies, and global transport paths. *Journal of Geophysical Research: Oceans*, 119(1), 313–331. <https://doi.org/10.1002/2013JC009356>
- Ito, T., Follows, M. J., & Boyle, E. A. (2004). Is AOU a good measure of respiration in the ocean? *Geophysical Research Letters*, 31(17), L17305. <https://doi.org/10.1029/2004GL020900>
- Jahnke, R. A. (1996). The global ocean flux of particulate organic carbon: Areal distribution and magnitude. *Global Biogeochemical Cycles*, 10(1), 71–88. <https://doi.org/10.1029/95gb03525>
- Jenkins, W. J. (1982). Oxygen utilization rates in North Atlantic subtropical gyre and primary production in oligotrophic systems. *Nature*, 300(5889), 246–248. <https://doi.org/10.1038/300246a0>
- Kalnay, E., Kanamitsu, M., Kistler, R., Collins, W., Deaven, D., Gandin, L., et al. (1996). The NMC/NCAR 40-year reanalysis project. *Bulletin of the American Meteorological Society*, 77(3), 437–471. [https://doi.org/10.1175/1520-0477\(1996\)077<0437:tnyrp>2.0.co;2](https://doi.org/10.1175/1520-0477(1996)077<0437:tnyrp>2.0.co;2)
- Karstensen, J., Stramma, L., & Visbeck, M. (2008). Oxygen minimum zones in the eastern tropical Atlantic and Pacific oceans. *Progress in Oceanography*, 77(4), 331–350. <https://doi.org/10.1016/j.pocean.2007.05.009>
- Keeling, R. F., K rtzinger, A., & Gruber, N. (2010). Ocean deoxygenation in a warming world. *Annual Review of Marine Science*, 2(1), 199–229. <https://doi.org/10.1146/annurev.marine.010908.163855>

- Keil, R. G., Neibauer, J. A., Biladeau, C., van der Elst, K., & Devol, A. H. (2016). A multiproxy approach to understanding the “enhanced” flux of organic matter through the oxygen-deficient waters of the Arabian Sea. *Biogeosciences*, *13*(7), 2077–2092. <https://doi.org/10.5194/bg-13-2077-2016>
- Koeve, W., & Kähler, P. (2016). Oxygen utilization rate (OUR) underestimates ocean respiration: A model study. *Global Biogeochemical Cycles*, *30*(8), 1166–1182. <https://doi.org/10.1002/2015GB005354>
- Kwon, E. Y., & Primeau, F. (2008). Optimization and sensitivity of a global biogeochemistry ocean model using combined in-situ DIC, alkalinity and phosphate data. *Journal of Geophysical Research*, *113*(C8), C08011. <https://doi.org/10.1029/2007JC004520>
- Laufkötter, C., John, J. G., Stock, C. A., & Dunne, J. P. (2017). Temperature and oxygen dependence of the remineralization of organic matter. *Global Biogeochemical Cycles*, *31*(7), 1038–1050. <https://doi.org/10.1002/2017GB005643>
- Letscher, R. T., & Moore, J. K. (2015). Preferential remineralization of dissolved organic phosphorus and non-Redfield DOM dynamics in the global ocean: Impacts on marine productivity, nitrogen fixation, and carbon export. *GBC*, *29*(3), 325–340. <https://doi.org/10.1002/2014GB004904>
- Matear, R. J., & Hirst, A. C. (2003). Long-term changes in dissolved oxygen concentrations in the ocean caused by protracted global warming. *Global Biogeochemical Cycles*, *17*(4), 1125. <https://doi.org/10.1029/2002GB001997>
- Matear, R. J., Hirst, A. C., & McNeil, B. I. (2000). Changes in dissolved oxygen in the Southern Ocean with climate change. *Geochemistry, Geophysics, Geosystems*, *1*(11), 2000GC000086. <https://doi.org/10.1029/2000gc000086>
- Moore, J. K., Fu, W., Primeau, F., Britten, G. L., Lindsay, K., Long, M., et al. (2018). Sustained climate warming drives declining marine biological productivity. *Science*, *359*(6380), 1139–1143. <https://doi.org/10.1126/science.aao6379>
- Najjar, R. G., Jin, X., Louanchi, F., Aumont, O., Caldeira, K., Doney, S. C., et al. (2007). Impact of circulation on export production, dissolved organic matter, and dissolved oxygen in the ocean: Results from Phase II of the Ocean Carbon-cycle Model Intercomparison Project (OCMIP-2). *Global Biogeochemical Cycles*, *21*(3), GB3007. <https://doi.org/10.1029/2006GB002857>
- Najjar, R. G., Sarmiento, J. L., & Toggweiler, J. R. (1992). Downward transport and fate of organic matter in the ocean: Simulations with a general circulation model. *Global Biogeochemical Cycles*, *6*(1), 45–76. <https://doi.org/10.1029/91gb02718>
- Olsen, A., Key, R. M., van Heuven, S., Lauvset, S. K., Velo, A., Lin, X., et al. (2016). The Global Ocean Data Analysis Project version 2 (GLODAPv2) – An internally consistent data product for the World Ocean. *Earth System Science Data*, *8*, 297–323. <https://doi.org/10.5194/essd-8-297-2016>
- Oschlies, A., & Kähler, P. (2004). Biotic contribution to air-sea fluxes of CO<sub>2</sub> and O<sub>2</sub> and its relation to new production, export production, and net community production. *Global Biogeochemical Cycles*, *18*(1), GB1015. <https://doi.org/10.1029/2003GB002094>
- Oschlies, A., Schulz, K. G., Riebesell, U., & Schmittner, A. (2008). Simulated 21st century's increase in oceanic suboxia by CO<sub>2</sub>-enhanced biotic carbon export. *Global Biogeochemical Cycles*, *22*(4), GB4008. <https://doi.org/10.1029/2007GB003147>
- Palter, J. B., & Trossman, D. S. (2018). The sensitivity of future ocean oxygen to changes in ocean circulation. *Global Biogeochemical Cycles*, *32*(5), 738–751. <https://doi.org/10.1002/2017GB005777>
- Pan, X., Achterberg, E. P., Sanders, R., Poulton, A. J., Oliver, K. I., & Robinson, C. (2014). Dissolved organic carbon and apparent oxygen utilization in the Atlantic Ocean. *Deep-Sea Research I*, *85*, 80–87. <https://doi.org/10.1016/j.dsr.2013.12.003>
- Pasquier, B., & Holzer, M. (2016). The plumbing of the global biological pump: Efficiency control through leaks, pathways, and time scales. *Journal of Geophysical Research*, *121*(8), 6367–6388. <https://doi.org/10.1002/2016JC011821>
- Pasquier, B., & Holzer, M. (2018). The number of past and future regenerations of iron in the ocean and its intrinsic fertilization efficiency. *Biogeosciences*, *15*(23), 7177–7203. <https://doi.org/10.5194/bg-15-7177-2018>
- Penn, J. L., Deutsch, C., Payne, J. L., & Sperling, E. A. (2018). Temperature-dependent hypoxia explains biogeography and severity of end-Permian marine mass extinction. *Science*, *362*(6419), eaat1327. <https://doi.org/10.1126/science.aat1327>
- Primeau, F. W. (2005). Characterizing transport between the surface mixed layer and the ocean interior with a forward and adjoint global ocean transport model. *Journal of Physical Oceanography*, *35*(4), 545–564. <https://doi.org/10.1175/JPO2699.1>
- Primeau, F. W., Holzer, M., & DeVries, T. (2013). Southern Ocean nutrient trapping and the efficiency of the biological pump. *Journal of Geophysical Research*, *118*(5), 2547–2564. <https://doi.org/10.1002/jgrc.20181>
- Schmittner, A., Oschlies, A., Matthews, H. D., & Galbraith, E. D. (2008). Future changes in climate, ocean circulation, ecosystems, and biogeochemical cycling simulated for a business-as-usual CO<sub>2</sub> emission scenario until year 4000 AD. *Global Biogeochemical Cycles*, *22*(1), GB1013. <https://doi.org/10.1029/2007GB002953>
- Sonnerup, R. E., Mecking, S., & Bullister, J. L. (2013). Transit time distributions and oxygen utilization rates in the Northeast Pacific Ocean from chlorofluorocarbons and sulfur hexafluoride. *Deep-Sea Research I*, *72*, 61–71. <https://doi.org/10.1016/j.dsr.2012.10.013>
- Sonnerup, R. E., Mecking, S., Bullister, J. L., & Warner, M. J. (2015). Transit time distributions and oxygen utilization rates from chlorofluorocarbons and sulfur hexafluoride in the Southeast Pacific Ocean. *Journal of Geophysical Research: Oceans*, *120*(5), 3761–3776. <https://doi.org/10.1002/2015JC010781>
- Sonnerup, R. E., Quay, P. D., & Bullister, J. L. (1999). Thermocline ventilation and oxygen utilization rates in the subtropical North Pacific based on CFC distributions during WOCE. *Deep-Sea Research, Part A: Oceanographic Research Papers I*, *46*(5), 777–805. [https://doi.org/10.1016/S0967-0637\(98\)00092-2](https://doi.org/10.1016/S0967-0637(98)00092-2)
- Stramma, L., Johnson, G. C., Firing, E., & Schmidtko, S. (2010). Eastern Pacific oxygen minimum zones: Supply paths and multidecadal changes. *Journal of Geophysical Research*, *115*(C9), C09011. <https://doi.org/10.1029/2009JC005976>
- Stramma, L., Johnson, G. C., Sprintall, J., & Mohrholz, V. (2008). Expanding oxygen-minimum zones in the tropical oceans. *Science*, *320*(5876), 655–658. <https://doi.org/10.1126/science.1153847>
- Teng, Y.-C., Primeau, F. W., Moore, J. K., Lomas, M. W., & Martiny, A. C. (2014). Global-scale variations of the ratios of carbon to phosphorus in exported marine organic matter. *Nature Geoscience*, *7*(12), 895–898. <https://doi.org/10.1038/NGEO2303>
- Vaquar-Sunyer, R., & Duarte, C. M. (2008). Thresholds of hypoxia for marine biodiversity. *Proceedings of the National Academy of Sciences*, *105*(40), 15452–15457. <https://doi.org/10.1073/pnas.0803833105>
- Wanninkhof, R. (1992). Relationship between wind speed and gas exchange over the ocean. *Journal of Geophysical Research*, *97*(C5), 7373–7382. <https://doi.org/10.1029/92jc00188>
- Wanninkhof, R., Park, G.-H., Takahashi, T., Sweeney, C., Feely, R., Nojiri, Y., et al. (2013). Global ocean carbon uptake: Magnitude, variability and trends. *Biogeosciences*, *10*(3), 1983–2000. <https://doi.org/10.5194/bg-10-1983-2013>
- Weber, T., & Bianchi, D. (2020). Efficient Particle Transfer to Depth in Oxygen Minimum Zones of the Pacific and Indian Oceans. *Frontiers of Earth Science*, *8*, 376. <https://doi.org/10.3389/feart.2020.00376>
- Westberry, T., Behrenfeld, M., Siegel, D., & Boss, E. (2008). Carbon-based primary productivity modeling with vertically resolved photoacclimation. *Global Biogeochemical Cycles*, *22*(2), GB2024. <https://doi.org/10.1029/2007GB003078>
- Whitney, F. A., Freeland, H. J., & Robert, M. (2007). Persistently declining oxygen levels in the interior waters of the eastern subarctic Pacific. *Progress in Oceanography*, *75*(2), 179–199. <https://doi.org/10.1016/j.pocan.2007.08.007>